Biogeosciences, 13, 5333–5355, 2016
www.biogeosciences.net/13/5333/2016/
doi:10.5194/bg-13-5333-2016

Biogeosciences Open Access EGU

Anaerobic oxidation of methane alters sediment records of sulfur, iron and phosphorus in the Black Sea

Matthias Egger[1], Peter Kraal[1], Tom Jilbert[1,a], Fatimah Sulu-Gambari[1], Célia J. Sapart[2,3], Thomas Röckmann[2], and Caroline P. Slomp[1]

[1]Department of Earth Sciences, Geochemistry, Faculty of Geosciences, Utrecht University, P.O. Box 80021, 3508 TA Utrecht, the Netherlands
[2]Institute for Marine and Atmospheric Research Utrecht (IMAU), Utrecht University, Princetonplein 5, 3584 CC Utrecht, the Netherlands
[3]Laboratoire de Glaciologie, Université Libre de Bruxelles, Brussels, Belgium
[a]now at: Department of Environmental Sciences, Faculty of Biological and Environmental Sciences, University of Helsinki, P.O. Box 65 (Viikinkaari 2a), 00014 Helsinki, Finland

Correspondence to: Matthias Egger (m.j.egger@uu.nl)

Received: 22 February 2016 – Published in Biogeosciences Discuss.: 10 March 2016
Revised: 7 August 2016 – Accepted: 17 August 2016 – Published: 23 September 2016

Abstract. The surface sediments in the Black Sea are underlain by extensive deposits of iron (Fe)-oxide-rich lake sediments that were deposited prior to the inflow of marine Mediterranean Sea waters ca. 9000 years ago. The subsequent downward diffusion of marine sulfate into the methane-bearing lake sediments has led to a multitude of diagenetic reactions in the sulfate-methane transition zone (SMTZ), including anaerobic oxidation of methane (AOM) with sulfate. While the sedimentary cycles of sulfur (S), methane and Fe in the SMTZ have been extensively studied, relatively little is known about the diagenetic alterations of the sediment record occurring below the SMTZ.

Here we combine detailed geochemical analyses of the sediment and porewater with multicomponent diagenetic modeling to study the diagenetic alterations below the SMTZ at two sites in the western Black Sea. We focus on the dynamics of Fe, S and phosphorus (P), and demonstrate that diagenesis has strongly overprinted the sedimentary burial records of these elements. In line with previous studies in the Black Sea, we show that sulfate-mediated AOM substantially enhances the downward diffusive flux of sulfide into the deep limnic deposits. During this downward sulfidization, Fe oxides, Fe carbonates and Fe phosphates (e.g., vivianite) are converted to sulfide phases, leading to an enrichment in solid-phase S and the release of phosphate to the porewater. Below the sulfidization front, high concentrations of dissolved ferrous Fe (Fe^{2+}) lead to sequestration of downward-diffusing phosphate as authigenic vivianite, resulting in a transient accumulation of total P directly below the sulfidization front.

Our model results further demonstrate that downward-migrating sulfide becomes partly re-oxidized to sulfate due to reactions with oxidized Fe minerals, fueling a cryptic S cycle and thus stimulating slow rates of sulfate-driven AOM ($\sim$ 1–100 pmol cm^{-3} d^{-1}) in the sulfate-depleted limnic deposits. However, this process is unlikely to explain the observed release of dissolved Fe^{2+} below the SMTZ. Instead, we suggest that besides organoclastic Fe oxide reduction and reactivation of less reactive Fe oxides by methanogens, AOM coupled to the reduction of Fe oxides may also provide a possible mechanism for the high concentrations of Fe^{2+} in the porewater at depth. Our results reveal that methane plays a key role in the diagenetic alterations of Fe, S and P records in Black Sea sediments. The downward sulfidization into the limnic deposits is enhanced through sulfate-driven AOM with sulfate, and AOM with Fe oxides may provide a deep source of dissolved Fe^{2+} that drives the sequestration of P in vivianite below the sulfidization front.

Published by Copernicus Publications on behalf of the European Geosciences Union.

1 Introduction

Anaerobic oxidation of methane (AOM), a process initially regarded as a biogeochemical curiosity, functions as an important sink for oceanic methane (CH_4) by consuming >90 % of all CH_4 produced in marine sediments (Knittel and Boetius, 2009; Reeburgh, 2007). Although recent studies indicate that the biological oxidation of CH_4 could be coupled to various additional electron acceptors such as nitrate and nitrite (Ettwig et al., 2010; Raghoebarsing et al., 2006) as well as metal oxides (Beal et al., 2009; Egger et al., 2015b; Riedinger et al., 2014; Scheller et al., 2016; Segarra et al., 2013; Sivan et al., 2011), sulfate (SO_4^{2-}) is commonly thought to be the dominant electron acceptor in anoxic marine systems (Knittel and Boetius, 2009; Reeburgh, 2007).

Nevertheless, a coupling between anaerobic CH_4 oxidation and iron (Fe) oxide reduction (Fe-AOM) could have a significant impact on sedimentary Fe cycling and related processes such as phosphorus (P) diagenesis, because of the 8 : 1 Fe–CH_4 stoichiometry of the reaction (Beal et al., 2009; Egger et al., 2015a; Rooze et al., 2016). Environmental conditions that favor Fe-AOM in marine systems are still poorly understood. The required co-occurrence of porewater CH_4 and abundant reducible Fe oxides suggests that Fe-AOM may occur in sediments that receive a relatively high input of Fe oxides compared to the in situ production of sulfide, which could allow a portion of Fe oxides to escape the conversion to authigenic Fe sulfides and to remain preserved in the methanogenic sediments below the zone of SO_4^{2-} reduction (Egger et al., 2015b; Riedinger et al., 2014; Rooze et al., 2016). In addition, perturbations inducing transient diagenesis such as anthropogenic eutrophication or climate change may also create diagenetic environments that are likely favorable for Fe-AOM, as they provide a mechanism for the burial of Fe-oxide-rich deposits below sulfidic sediment layers (Egger et al., 2015b; Riedinger et al., 2014).

The Black Sea represents a good example of a sedimentary system in which transient diagenesis associated with postglacial sea-level rise has led to the accumulation of sulfidic sediments above Fe-oxide-rich deposits. Here, the establishment of a connection to the Mediterranean Sea through the shallow Bosporus around 9000 years ago (Degens and Ross, 1974; Soulet et al., 2011) led to the inflow of marine waters into a freshwater basin, resulting in permanent salinity/density stratification and in the development of euxinic conditions (i.e., free dissolved sulfide present in the bottom water), making the current Black Sea the largest permanently anoxic basin on Earth.

In the absence of oxygen and metal oxides, SO_4^{2-} reduction is the dominant benthic mineralization process of organic matter in Black Sea surface sediments below the chemocline (∼ 100 m depth; Jørgensen et al., 2001; Thamdrup et al., 2000). At present, SO_4^{2-} penetrates through the modern coccolith ooze (Unit I) and the marine sapropel (Unit II) sediments and a few meters into the Upper Pleistocene freshwater deposits (Unit III; Arthur and Dean, 1998; Degens and Ross, 1974; Jørgensen et al., 2004). Below the SO_4^{2-}-bearing zone, methanogenesis takes over as the dominant process of organic matter degradation, resulting in the buildup of CH_4 in the porewater at depth.

Interactions between the cycles of sulfur (S) and CH_4 in Black Sea sediments have been extensively studied during recent years (Holmkvist et al., 2011b; Jørgensen et al., 2001, 2004; Knab et al., 2009; Leloup et al., 2007) and AOM coupled to SO_4^{2-} reduction (SO_4-AOM) was found to account for an estimated 7–18 % of total SO_4^{2-} reduction in these sediments (Jørgensen et al., 2001). The production of sulfide in the sulfate-methane transition zone (SMTZ) as a result of SO_4-AOM represents the main source of porewater sulfide at depth in the sediment. This intensified production of sulfide drives an enhanced downward diffusive flux of sulfide into the deep limnic deposits of Unit III, forming a distinct diagenetic sulfidization front recognized as a black band or a series of bands owing to the conversion of Fe oxides to Fe sulfides (Berner, 1974; Jørgensen et al., 2004; Neretin et al., 2004).

At present, the impact of the downward-migrating sulfidization front on sedimentary P, a key nutrient for marine phytoplankton, and the potential role of Fe-mediated AOM in the deep limnic deposits remain largely unknown. A buildup of ferrous Fe (Fe^{2+}) in the porewater at depth, as found in previous studies (Holmkvist et al., 2011b; Jørgensen et al., 2004; Knab et al., 2009), could indicate ongoing Fe reduction in the CH_4-bearing deep limnic sediments and thus a potential coupling between AOM and Fe oxide reduction. The sediment records investigated up to now, however, do not extend deep enough to allow the sedimentary cycling of Fe and related biogeochemical processes below the sulfidization front to be investigated. In particular, the presence of abundant dissolved Fe^{2+} combined with a potential release of porewater phosphate (HPO_4^{2-}) during reductive dissolution of Fe oxides may be conducive to the formation of reduced Fe(II)–P minerals such as vivianite ($Fe_3(PO)_4 \times 8H_2O$) below the sulfidization front (Egger et al., 2015a; Hsu et al., 2014; März et al., 2008; Sivan et al., 2011). Post-depositional diagenetic alterations as a result of downward sulfidization could therefore overprint burial records of P in the Upper Pleistocene deposits.

In this study, we combine detailed geochemical analyses of the sediment and porewater with multicomponent diagenetic modeling to study the diagenetic alterations below the lake–marine transition at two sites in the western Black Sea. Focusing on the dynamics of S, Fe and P, we demonstrate that AOM coupled to SO_4^{2-} reduction enhances the downward sulfidization and associated dissolution of Fe oxides, Fe carbonates and vivianite, supporting earlier findings of an SO_4-AOM enhanced downward sulfidization in Black Sea sediments (Jørgensen et al., 2001). Below the sulfidization front, downward-diffusing HPO_4^{2-} precipitates as vivianite by re-

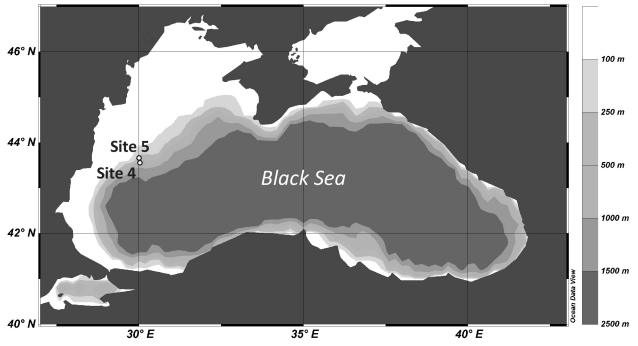

Figure 1. Map showing the locations of site 4 (43°40.6′ N, 30°7.5′ E; 377 m b.s.s.) and site 5 (43°42.6′ N, 30°6.1′ E; 178 m b.s.s.), sampled in June 2013.

action with the abundant dissolved Fe^{2+}. We propose that organoclastic Fe oxide reduction, reactivation of less reactive Fe oxides by methanogens (Sivan et al., 2016) and/or AOM coupled to the reduction of Fe oxides are the key processes explaining the high concentrations of dissolved Fe^{2+} at depth in the sediment. Trends in total S and P with depth are significantly altered by the above-mentioned reactions, highlighting that diagenesis may strongly overprint burial records of these elements below a lake–marine transition.

2 Materials and methods

2.1 Sample collection

2.1.1 Gravity core sampling

Sediment samples were taken at two slope sites in the western Black Sea during a cruise in June 2013 with R/V *Pelagia*. Gravity cores containing ∼ 7 m of sediment were collected at sites 4 (43°40.6′N, 30°7.5′ E; 377 m below sea surface; m b.s.s.) and 5 (43°42.6′ N, 30°6.1′ E; 178 m b.s.s.; Fig. 1), both situated below the current chemocline (∼ 100 m water depth). The core liners were pre-drilled with 2 cm diameter holes in two rows of 10 cm resolution on opposing sides of the tube, offset by 5 cm and taped prior to coring. Upon recovery, the liners were cut into 1 m sections, transferred to a temperature-controlled container set at in situ bottom water temperature (11 °C) and secured vertically. Subsequently, the taped holes were cut open and a cut-off syringe was inserted horizontally directly after opening each hole.

From one series of holes, 10 mL of wet sediment was extracted at 20 cm resolution and immediately transferred into a 65 mL glass bottle filled with saturated NaCl solution for CH_4 analysis. The NaCl solution was topped up after addition of the sample, ensuring that no air bubbles remained. Each bottle was sealed with a black rubber stopper and a screw cap and was subsequently stored upside down at room temperature. From the second series of holes, 20 mL sediment was extracted at 20 cm resolution, sealed with parafilm that was tightly closed with an elastic band, and directly inserted into a nitrogen (N_2)-purged glove box. Subsequently, the sediment was transferred into a 50 mL centrifuge tube and centrifuged (4500 rpm; 30 min). The supernatant from each centrifuged sample was filtered through 0.45 µm pore size disposable filters via 20 mL plastic syringes in the glove box and collected in 15 mL centrifuge tubes. The sediment fraction was stored frozen (−20 °C) for solid-phase analysis. Filtered porewater samples were subsampled under N_2 for analysis of dissolved HPO_4^{2-}, ammonium (NH_4^+), dissolved inorganic carbon (DIC), Fe, manganese (Mn), SO_4^{2-} and sulfide ($\sum H_2S = H_2S + HS^-$; see Sect. 2.2). Additional samples of 10 mL of sediment were collected at approximately 50 cm resolution and transferred into pre-weighed 15 mL glass vials to determine porosity from gravimetric water loss.

2.1.2 Multicore sampling

To sample the surface sediment, sediment cores (30–60 cm of sediment and at least 10 cm of overlying water) were recovered using an octopus multicorer (core diameter 10 cm). After recovery, the cores were stoppered at the base and at the top and immediately transported to a temperature-controlled container (11 °C). One multicore from each cast was predrilled with 2 cm diameter holes in two rows at 10 cm resolution on opposing sides of the tube, offset by 5 cm, and taped prior to coring. These holes were sampled for CH_4 as described for the gravity cores. Another core was directly inserted into a N_2-purged glove box through an airtight hole in the base. A bottom water sample was collected using a 20 mL plastic syringe and the remaining bottom water was removed with a Tygon tube. Subsequently, the core was sliced anoxically with decreasing resolution at depth, i.e., 0.5 cm resolution for the first 0–2 cm, 1 cm resolution between 2–10 cm, 2 cm resolution between 10–20 cm and 4 cm resolution for the rest of the core (> 20 cm). For each slice a subsample was placed in a pre-weighed 15 mL glass vial for water content and solid-phase analysis and stored under N_2 in airtight jars at −20 °C. A second subsample was transferred to a 50 mL centrifuge tube and centrifuged (4500 rpm; 30 min). Both the supernatant water from each centrifuged sample and the bottom water sample were subsequently processed as described for the gravity cores.

Visual alignment of the porewater profiles from the multicores with those of the gravity cores showed that the first ∼ 20 to 30 cm of sediment was lost during long coring. At site 5, the sediment in the multicore consisted of a gray and homogeneous turbidite below 1.5 cm depth. The depth for the gravity core at site 5 was thus corrected for the loss of the marine deposits, which were previously reported to be about 50 cm thick at a site in close proximity to site 5 (43°42.63′ N, 30°6.12′ E; 181 m b.s.s.; Jørgensen et al., 2004).

2.2 Porewater subsampling

A subsample of 0.5 mL was immediately transferred into a glass vial containing 1.5 mL of 8 M NaOH solution for analysis of dissolved sulfide. Subsamples of total dissolved Fe and Mn, which are assumed to represent Fe(II) and Mn(II), were acidified with 10 µL 35 % Suprapur® HCl per mL of subsample. Note, however, that the dissolved (< 0.45 µm) Fe and Mn pools likely consist of a mixture of truly dissolved (aqueous) Fe and Mn species, as well as organically complexed, colloidal and nanoparticulate Fe and Mn species (Raiswell and Canfield, 2012). Another 1 mL of porewater for HPO_4^{2-} analysis was acidified with 4 µL 5 M HCl. Porewater SO_4^{2-} was analyzed with ion chromatography (IC) in a 10-fold diluted sample (0.15 mL of porewater with 1.35 mL of de-oxygenated UHQ water). Subsamples for DIC analysis (0.5 mL) were collected in glass vials (4.9 mL) to which 4.4 mL of 25 g L^{-1} NaCl solution was added, making sure that no headspace remained. Aliquots of the remaining porewater were used for the measurement of alkalinity (determined on board by titrating 1 mL of untreated subsample with 0.01 M HCl; results presented in the Supplement) and NH_4^+. All subsamples were stored at 4 °C and brought to room temperature just before analysis. Subsampling for sulfide was performed immediately after filtration, and all other subsampling was performed within 4 h of core recovery.

Porewater subsamples of HPO_4^{2-}, DIC and sulfide were directly analyzed colorimetrically on board on two separate QuAAtro (SEAL Analytical, Germany) auto analyzers. HPO_4^{2-} was measured at 880 nm after the formation of molybdophosphate complexes (Murphy and Riley, 1962). Samples for DIC were acidified online after being oxidized by H_2O_2 and analyzed as described by Stoll et al. (2001). To keep the dissolved sulfide in the nonvolatile HS^- form under alkaline conditions, 1.5 mL of 8 mM NaOH was added to the sulfide samples, which were subsequently analyzed using the methylene blue method as described by Grasshoff (1969). Subsamples of dissolved Fe and Mn were analyzed onshore by ICP-OES (Perkin Elmer Optima 3000 Inductively Coupled Plasma – Optimal Emission Spectroscopy). For the analysis of porewater CH_4, a volume of 10 mL N_2 was injected into the CH_4 serum flasks (while a needle inserted through the septum allowed 10 mL of water to escape) to create a headspace from which a subsample was collected with a gas-tight syringe. Subsequently, CH_4 concentrations were determined in the home laboratory after injection into a Thermo Finnigan TRACE™ gas chromatograph (Flame Ionization Detector). $\delta^{13}C$–CH_4 and δD–CH_4 (D, deuterium) were analyzed by Continuous Flow Isotope Ratio Mass Spectrometry (CF-IRMS) as described in detail in Brass and Röckmann (2010) and Sapart et al. (2011).

2.3 Bulk sediment analysis

Sediment samples were freeze-dried, powdered and ground in an agate mortar in an argon (Ar)-filled glove box and split into oxic and anoxic fractions. Samples from the oxic fraction were used for total elemental and organic carbon (C_{org}) analyses under normal atmospheric conditions, whereas anoxic splits for sediment P and Fe speciation were kept under an inert, oxygen-free Ar or N_2 atmosphere at all times to avoid oxidation artifacts (Kraal and Slomp, 2014; Kraal et al., 2009).

2.3.1 Total elemental composition and organic carbon

A split of ∼ 125 mg of freeze-dried sediment was dissolved overnight in 2.5 mL HF (40 %) and 2.5 mL of $HClO_4$–HNO_3 mixture, in a closed Teflon bomb at 90 °C. The acids were then evaporated at 160 °C, and the resulting gel was dissolved overnight in 1 M HNO_3 at 90 °C. Total elemental concentrations in the 1 M HNO_3 solutions were determined by ICP-OES. A second split of 0.3 g freeze-dried sediment was used to determine the C_{org} content using an elemental analyzer (Fison Instruments model NA 1500 NCS) after carbonate removal from the sediment with two washes with 1 M HCl (4 and 12 h) followed by two washes with UHQ water and subsequent drying of the samples (Van Santvoort et al., 2002).

2.3.2 Sediment P fractionation

To determine the solid-phase partitioning of P, aliquots of 0.1 g dried sediment were subjected to the SEDEX sequential extraction procedure after Ruttenberg (1992), as modified by Slomp et al. (1996b), but including the first $MgCl_2$ step (Table 1). Sediment P was fractionated as follows: (i) exchangeable P ("P_{exch}", extracted by 1 M $MgCl_2$, pH 8, 0.5 h), (ii) Fe-associated P ("P_{Fe}", extracted by citrate–bicarbonate–dithionite (CDB), buffered to pH 7.5 with Na citrate/Na bicarbonate, 8 h, followed by 1 M $MgCl_2$, pH 8, 0.5 h), (iii) authigenic Ca–P ("$P_{authi\ Ca–P}$", including carbonate fluorapatite, biogenic hydroxyapatite and $CaCO_3$-bound P, extracted by 1 M Na acetate solution, buffered to pH 4 with acetic acid, 6 h, followed by 1 M $MgCl_2$, pH 8, 0.5 h), (iv) detrital Ca–P ("P_{detr}", extracted by 1 M HCl, 24 h) and (v) organic P ("P_{org}", after ashing at 550 °C for 2 h, extracted by 1 M HCl, 24 h). The $MgCl_2$ washes in steps ii and iii were to ensure that any HPO_4^{2-} re-adsorbed during CDB or acetate extraction was removed and included in the pools of Fe-associated P and authigenic Ca–P, respectively. Sediments were shielded from oxygen inside an Ar-filled glovebox until step 3 of the SEDEX procedure to eliminate the potential conversion of Ca–P to Fe-bound P due to pyrite oxidation upon oxygen exposure (Kraal and Slomp, 2014; Kraal et al., 2009). Dissolved HPO_4^{2-} in the CDB solution was analyzed by ICP-OES. For all other solutions, HPO_4^{2-} was determined col-

Table 1. Overview of the sequential P, Fe and S fractionation methods used in this study.

Step and code	Extractant, extraction time	Target phase
P fractionation (modified from Ruttenberg (1992); done for site 4 (MC & GC) and site 5 (MC & GC))		
1 P_{exch}	1 M $MgCl_2$, pH 8, 0.5 h	Exchangeable P
2*P_{Fe}	25 g L^{-1} Na dithionite, pH 7.5, 8 h	Fe-associated P
3*$P_{authi\ Ca–P}$	Na acetate buffer, pH 4, 6 h	P in authigenic and biogenic Ca–P minerals and $CaCO_3$
4 P_{detr}	1 M HCl, 24 h	Detrital P
5 P_{org}	Ashing at 550 °C (2h), then 1 M HCl, 24 h	Organic P
Fe fractionation (after Poulton and Canfield (2005); done for site 4 (MC & GC) and site 5 (MC))		
1 Fe_{carb}	1 M Na acetate, pH 4.5, 24 h	Carbonate-associated Fe
2 Fe_{ox1}	1 M hydroxylamine-HCl, 24 h	Amorphous Fe oxides (ferrihydrite)
3 Fe_{ox2}	50 g L^{-1} Na dithionite, pH 4.8, 2 h	Crystalline Fe oxides (goethite, hematite)
4 Fe_{mag}	0.2 M ammonium oxalate/0.17 M oxalic acid, 2 h	Recalcitrant Fe oxides (mostly magnetite)
Fe fractionation (modified from Claff et al. (2010); done for site 4 (MC & GC) and site 5 (MC))		
1 $Fe(II)_{HCl}$	1 M HCl, 4 h	Labile Fe (carbonates, poorly ordered sulfides)
2 $Fe(III)_{HCl}$	1 M HCl, 4 h	Labile Fe (easily reducible oxides)
3 $Fe(III)_{CDB}$	50 g L^{-1} Na dithionite, pH 4.8, 4 h	Crystalline Fe oxides
4 Fe_{pyrite}	Concentrated HNO_3, 2 h	Pyrite (FeS_2)
S fractionation (after Burton et al. (2008); done for site 4 (MC) and site 5 (MC & GC))		
1 AVS	6 M HCl, 24 h	S in Fe monosulfides (FeS)
2 CRS	Acidic chromous chloride solution, 48 h	S in pyrite (FeS_2)

* These steps were followed by a wash step with 1 M $MgCl_2$, which was added to the corresponding step. MC is the multicore and GC is the gravity core.

orimetrically (Strickland and Parsons, 1972) on a Shimadzu spectrophotometer using the ammonium heptamolybdate – ascorbic acid method.

2.3.3 Sediment Fe fractionation

Sediment Fe was fractionated into (i) carbonate-associated Fe ("Fe_{carb}", including siderite and ankerite, extracted by 1 M Na acetate brought to pH 4.5 with acetic acid, 24 h), (ii) easily reducible (amorphous) oxides ("Fe_{ox1}", including ferrihydrite and lepidocrocite, extracted by 1 M hydroxylamine-HCl, 24 h), (iii) reducible (crystalline) oxides ("Fe_{ox2}", including goethite, hematite and akagenéite, extracted by Na–dithionite buffer, pH 4.8, 2 h) and (iv) Fe in recalcitrant oxides (mostly magnetite, "Fe_{mag}", extracted by 0.2 M ammonium oxalate/0.17 M oxalic acid solution, 2 h), according to Poulton and Canfield (2005), using a 50 mg aliquot of dried sediment (Table 1). An additional aliquot of 50 mg was subjected to an adapted sequential extraction procedure after Claff et al. (2010), separating labile Fe(II) ("$Fe(II)_{HCl}$") and Fe(III) ("$Fe(III)_{HCl}$") using 1 M HCl (4 h) from crystalline Fe oxide minerals ("$Fe(II)_{CDB}$", Na–dithionite buffer, pH 4.8, 4 h) and from pyrite ("Fe_{pyrite}", concentrated nitric acid, 2 h), for all multicores as well as for the long core at site 4 (Table 1).

At site 4 (multicore only) and 5 (multicore and gravity core), aliquots of 0.5 g dried sediment were used to sequentially determine the amount of FeS (acid volatile sulfur, "AVS", using 6 M HCl) and FeS_2 (chromium reducible sulfur, "CRS", using acidic chromous chloride solution) via the passive diffusion method described by Burton et al. (2008) using iodometric titration of the ZnS formed in the alkaline Zn acetate traps to quantify AVS and CRS (Table 1).

2.4 Diagenetic model

2.4.1 General form

A multicomponent transient diagenetic model was developed for site 4 based on existing diagenetic models (Reed et al., 2011a, b; Rooze et al., 2016) to gain a better understanding of the transient diagenesis in Black Sea sediments and to investigate the potential for Fe-AOM as a source of porewater Fe^{2+} at depth. The model describes the cycling of dissolved and particulate chemical species in a 1-D sediment column (Berner, 1980). A total of 25 different chemical species (Table 2) were subjected to a suite of biogeochemical reactions (Table 3) and vertical transport through burial, as well as molecular diffusion for dissolved species (Boudreau, 1997; Soetaert et al., 1996; Wang and Van Cappellen, 1996). The general diagenetic equations for solid (Eq. 1) and dissolved

Table 2. Chemical species included in the diagenetic model.

Species	Notation	Type
Organic matter[a]	$OM^{\alpha,\beta,\gamma}$	Solid
Iron oxides[a]	$Fe(OH)_3^{\alpha,\beta,\gamma}$	Solid
Iron monosulfide	FeS	Solid
Pyrite	FeS_2	Solid
Siderite	$FeCO_3$	Solid
Elemental sulfur	S_0	Solid
Iron-oxide-bound phosphorus	$Fe_{ox}P$	Solid
Vivianite	$Fe_3(PO_4)_2$	Solid
Organic phosphorus	P_{org}	Solid
Authigenic (Ca) phosphorus	$P_{authi\ Ca\text{-}P}$	Solid
Detrital phosphorus	P_{Detr}	Solid
Chloride	Cl^-	Solute
Oxygen	O_2	Solute
Sulfate	SO_4^{2-}	Solute
Iron	Fe^{2+}	Solute
Hydrogen sulfide[b]	$\sum H_2S$	Solute
Methane	CH_4	Solute
Ammonium[b]	$\sum NH_4^+$	Solute
Nitrate	NO_3^-	Solute
Phosphate	$\sum HPO_4^{2-}$	Solute
Dissolved inorganic carbon	DIC	Solute

[a] There are three types of species: reactive (α), less reactive (β) and refractory (γ). [b] $\sum$ denotes that all species of an acid are included.

species (Eq. 2) are, respectively,

$$(1-\phi)\frac{\partial C_S}{\partial t} = -(1-\phi)v\frac{\partial C_S}{\partial x} + \sum R_S \quad (1)$$

$$\phi\frac{\partial C_{aq}}{\partial t} = \phi D'\frac{\partial^2 C_{aq}}{\partial x^2} - \phi u\frac{\partial C_{aq}}{\partial x} + \sum R_{aq}, \quad (2)$$

where C_S is the concentration of the solid species ($mol\,L^{-1}$; mass per unit volume of solids), C_{aq} the concentration of the dissolved species ($mol\,L^{-1}$; mass per unit volume of porewater), t is time (yr), ϕ the sediment porosity, x the distance from the sediment–water interface (cm), D' the diffusion coefficients of dissolved species in the sediment ($cm^2\,yr^{-1}$) adjusted for the considered setting (Supplement Table S1; Boudreau, 1997) and corrected for the tortuosity in the porous medium (Boudreau, 1996; see Supplement). $\sum R_S$ and $\sum R_{aq}$ are the net reaction rates of the solid and dissolved species from the chemical reactions they participate in (Table 3), and v and u the advective velocities ($cm\,yr^{-1}$) of the solid and the dissolved species, respectively. Porosity and advective velocities were described by depth-dependent functions to account for sediment compaction (Meysman et al., 2005; Reed et al., 2011a; see Supplement Fig. S1).

Reactions considered by the model and corresponding reaction equations are given in Tables 3 and 4, respectively, and are divided into primary redox reactions and other biogeochemical reactions, including various mineral formation and dissolution reactions (Reed et al., 2011a, b; Rooze et al., 2016). Corresponding reaction parameters were mostly taken from the literature or, if these were not available or no fit to the data could be obtained with existing parameter ranges, constrained using the extensive geochemical dataset for site 4 (Table 5). A model sensitivity analysis for key parameters is provided in the Supplement (Figs. S2 and S3).

To account for differences in reactivity and crystallinity between different species, organic matter and Fe oxides are divided into three different pools, representing highly reactive (α), less reactive (β) and nonreactive (i.e., inert; γ) phases. For the Fe oxides, only the α phase is used by organoclastic Fe reduction (Table 3), while the β phase is also used by Fe-AOM. This assumption was made to test whether the porewater and sediment profiles observed in the Black Sea can be reproduced with Fe-AOM as the main Fe reduction pathway at depth. In addition, it allows an assessment of the potential impact of Fe-AOM on sedimentary CH_4 cycling. Note that, as a consequence of the exclusion of organoclastic Fe reduction at depth, the model results should not be interpreted as proof for Fe-AOM but rather imply that it is a possible mechanism.

The succession of oxidants during organic matter decomposition (Froelich et al., 1979) is described by means of Monod kinetics (Table 4), whereby those oxidants with the highest metabolic free energy yield are used preferentially until they become limiting and the oxidant with the next highest energy yield is used (Berg et al., 2003; Boudreau, 1996; Reed et al., 2011b; Rooze et al., 2016; Wang and Van Cappellen, 1996). Oxidants considered by the model are (in descending order of energy yield) O_2, nitrate (NO_3^-), Fe oxides and SO_4^{2-}. Once these oxidants are exhausted, organic matter remineralization occurs by methanogenesis. Corresponding limiting concentrations for the oxidants are taken from Reed et al. (2011a; Table 5). In addition, an attenuation factor, Ψ, is used to slow down anaerobic organic matter degradation through SO_4^{2-} reduction and methanogenesis, thus allowing for better preservation of organic matter under anoxic bottom water conditions (Moodley et al., 2005; Reed et al., 2011a, b).

Cycling of S is simulated using five different chemical species, i.e., Fe monosulfides (FeS), pyrite (FeS_2), elemental S (S_0), dissolved sulfide and porewater SO_4^{2-} (Table 2), combined in a network of various biogeochemical reactions (Table 3). The CH_4 cycle includes CH_4 production from organic matter and from DIC (i.e., CO_2), as well as CH_4 oxidation coupled to the reduction of O_2, SO_4^{2-} and $Fe(OH)_3$ (Table 3). For AOM a bimolecular rate equation was used (Table 4), which is the most common way to parameterize AOM in reactive transport models (Regnier et al., 2011) and allows the use of largely unknown half-saturation constants, in particular for the putative Fe-AOM pathway, to be avoided. Although Mn oxides have also been suggested to be a thermodynamically favorable electron acceptor for AOM (Beal et al., 2009), they were not included in the model because of

Table 3. Reaction pathways and stoichiometries implemented in the diagenetic model.

Primary redox reactions[1]	
$OM^{\alpha,\beta} + aO_2 \rightarrow aCO_2 + bNH_4^+ + cH_3PO_4 + aH_2O$	R1
$OM^{\alpha,\beta} + \frac{4a}{5}NO_3^- + \frac{4a}{5}H^+ \rightarrow aCO_2 + bNH_4^+ + cH_3PO_4 + \frac{2a}{5}N_2 + \frac{7a}{5}H_2O$	R2
$OM^{\alpha,\beta} + 4aFe(OH)_3^{\alpha} + 4a\chi^{\alpha}Fe_{ox}P + 12aH^+ \rightarrow aCO_2 + bNH_4^+ + (c+4a\chi^{\alpha})H_3PO_4 + 4aFe^{2+} + 13aH_2O$	R3
$OM^{\alpha,\beta} + \frac{a}{2}SO_4^{2-} + aH^+ \rightarrow aCO_2 + bNH_4^+ + cH_3PO_4 + \frac{a}{2}H_2S + aH_2O$	R4
$OM^{\alpha,\beta} \rightarrow \frac{a}{2}CO_2 + bNH_4^+ + cH_3PO_4 + \frac{a}{2}CH_4$	R5
$CO_2 + 4H_2 \rightarrow CH_4 + 2H_2O$	R6
Secondary redox and other reaction equations[2]	
$2O_2 + NH_4^+ + 2HCO_3^- \rightarrow NO_3^- + 2CO_2 + 3H_2O$	R7
$O_2 + 4Fe^{2+} + 8HCO_3^- + 2H_2O + 4\chi^{\alpha}H_2PO_4^- \rightarrow 4Fe(OH)_3^{\alpha} + 4\chi^{\alpha}Fe_{ox}P + 8CO_2$	R8
$2O_2 + FeS \rightarrow SO_4^{2-} + Fe^{2+}$	R9
$7O_2 + 2FeS_2 + 2H_2O \rightarrow 4SO_4^{2-} + 2Fe^{2+} + 4H^+$	R10
$2O_2 + H_2S + 2HCO_3^- \rightarrow SO_4^{2-} + 2CO_2 + 2H_2O$	R11
$2O_2 + CH_4 \rightarrow CO_2 + 2H_2O$	R12
$2Fe(OH)_3^{\alpha} + 2\chi^{\alpha}Fe_{ox}P + H_2S + 4CO_2 \rightarrow 2Fe^{2+} + 2\chi^{\alpha}H_2PO_4^- + S_0 + 4HCO_3^- + 2H_2O$	R13
$2Fe(OH)_3^{\beta} + 2\chi^{\beta}Fe_{ox}P + H_2S + 4CO_2 \rightarrow 2Fe^{2+} + 2\chi^{\beta}H_2PO_4^- + S_0 + 4HCO_3^- + 2H_2O$	R14
$Fe^{2+} + H_2S \rightarrow FeS + 2H^+$	R15
$FeS + H_2S \rightarrow FeS_2 + H_2$	R16
$4S_0 + 4H_2O \rightarrow 3H_2S + SO_4^{2-} + 2H^+$	R17
$FeS + S_0 \rightarrow FeS_2$	R18
$SO_4^2 + CH_4 + CO_2 \rightarrow 2HCO_3^- + H_2S$	R19
$CH_4 + 8Fe(OH)_3^{\alpha,\beta} + 8\chi^{\alpha,\beta}Fe_{ox}P + 15H^+ \rightarrow HCO_3^- + 8Fe^{2+} + 8\chi^{\alpha,\beta}H_2PO_4^- + 21H_2O$	R20
$Fe(OH)_3^{\alpha} + \left(\chi^{\alpha} - \chi^{\beta}\right)Fe_{ox}P \rightarrow Fe(OH)_3^{\beta} + \left(\chi^{\alpha} - \chi^{\beta}\right)H_2PO_4^-$	R21
$Fe(OH)_3^{\beta} + \left(\chi^{\beta} - \chi^{\gamma}\right)Fe_{ox}P \rightarrow Fe(OH)_3^{\gamma} + \left(\chi^{\beta} - \chi^{\gamma}\right)H_2PO_4^-$	R22
$3Fe^{2+} + 2HPO_4^{2-} \rightarrow Fe_3(PO_4)_2 + 2H^+$	R23
$Fe^{2+} + CO_3^{2-} \rightarrow FeCO_3$	R24
$FeCO_3 + H_2S \rightarrow FeS + HCO_3^- + H^+$	R25
$Fe_3(PO_4)_2 + 3H_2S \rightarrow 3FeS + 2HPO_4^{2-} + 4H^+$	R26

[1] Organic matter (OM) is of the form $(CH_2O)_a(NH_4^+)_b(H_3PO_4)_c$, with "a" = 1, "b" = 1/16 and "c" = 1/106. Under anoxic bottom water conditions, "c" reduces to 0.25 to account for the preferential regeneration of P (e.g., Ingall et al., 1993). [2] $\chi^{\alpha,\beta,\gamma}$ refers to the P : Fe ratio of $Fe(OH)_3^{\alpha,\beta,\gamma}$ (see Table S1). R6 is the CH_4 production from DIC (i.e., CO_2); R7 is the nitrification; R8 is the $Fe(OH)_3$ formation; R9 is the FeS oxidation; R10 is the FeS_2 oxidation; R11 is the H_2S oxidation; R12 is the aerobic CH_4 oxidation; R13 and R14 are the $Fe(OH)_3$ reduction by H_2S; R15 is the FeS formation; R16 is the pyrite formation (H_2S pathway); R17 is the S_0 disproportionation; R18 is the pyrite formation (polysulfide pathway); R19 is the SO_4-AOM; R20 is the Fe-AOM; R21 is the conversion (i.e., crystallization) from α to β phase; R22 is the crystallization from β to γ phase; R23 is the vivianite formation; R24 is the siderite precipitation; R25 is the conversion from siderite to FeS; R26 is the vivianite dissolution by dissolved sulfide.

the relatively low Mn concentrations ($\sim 15\,\mu mol\,g^{-1}$ for total sedimentary Mn and $< 30\,\mu M$ for dissolved Mn^{2+}; Figs. S2 and S3) when compared to Fe and the likely presence of most of the Mn in the form of Mn carbonates.

The P forms included in the model are porewater HPO_4^{2-}, authigenic Ca–P, organic P and detrital P, as well as Fe-bound P, i.e., P associated with Fe oxides and P in vivianite (Table 2). The removal of dissolved Fe^{2+} through formation of the Fe minerals FeS, siderite ($FeCO_3$) and vivianite is also included in the model (Table 3). Mass balances for all chemical species included in the model are given in Table S2.

The boundary conditions at the sediment surface were specified as time-dependent depositional fluxes for the particulate components and as fixed bottom water concentrations for the dissolved species, while a zero gradient boundary condition was set for all chemical species at the base of the model domain (Fig. 2 and Table S3). To avoid potential interferences of the lower boundary conditions with the model results in the upper sediments (see Fig. S6), the model depth was set to 3000 cm and divided into 500 grid cells. The thickness of the upper layer was set at 1 cm, and the thickness of the following grid layers increased exponentially to ~ 6 cm at 800 cm depth and to ~ 18 cm at 3000 cm depth. In this paper, only the upper 800 cm are shown. However, all profiles extending over the full depth range are provided in the Supplement file (Figs. S5 and S7). The model code was written in R using the marelac geochemical dataset package (Soetaert et al., 2010) and the ReacTran package

Table 4. Reaction equations implemented in the model.

Primary redox reaction equations	
$R_1 = k_{\alpha,\beta}\mathrm{OM}^{\alpha,\beta}\left(\frac{[\mathrm{O_2}]}{\mathrm{K_{O_2}}+[\mathrm{O_2}]}\right)$	(E1)
$R_2 = k_{\alpha,\beta}\mathrm{OM}^{\alpha,\beta}\left(\frac{[\mathrm{NO_3^-}]}{\mathrm{K_{NO_3^-}}+[\mathrm{NO_3^-}]}\right)\left(\frac{\mathrm{K_{O_2}}}{\mathrm{K_{O_2}}+[\mathrm{O_2}]}\right)$	(E2)
$R_3 = k_{\alpha,\beta}\mathrm{OM}^{\alpha,\beta}\left(\frac{[\mathrm{Fe(OH)_3^\alpha}]}{\mathrm{K_{Fe(OH)_3^\alpha}}+[\mathrm{Fe(OH)_3^\alpha}]}\right)\left(\frac{\mathrm{K_{NO_3^-}}}{\mathrm{K_{NO_3^-}}+[\mathrm{NO_3^-}]}\right)\left(\frac{\mathrm{K_{O_2}}}{\mathrm{K_{O_2}}+[\mathrm{O_2}]}\right)$	(E3)
$R_4 = \Psi k_{\alpha,\beta}\mathrm{OM}^{\alpha,\beta}\left(\frac{[\mathrm{SO_4^{2-}}]}{\mathrm{K_{SO_4^{2-}}}+[\mathrm{SO_4^{2-}}]}\right)\left(\frac{\mathrm{K_{Fe(OH)_3^\alpha}}}{\mathrm{K_{Fe(OH)_3^\alpha}}+[\mathrm{Fe(OH)_3^\alpha}]}\right)\left(\frac{\mathrm{K_{NO_3^-}}}{\mathrm{K_{NO_3^-}}+[\mathrm{NO_3^-}]}\right)\left(\frac{\mathrm{K_{O_2}}}{\mathrm{K_{O_2}}+[\mathrm{O_2}]}\right)$	(E4)
$R_5 = \Psi k_{\alpha,\beta}\mathrm{OM}^{\alpha,\beta}\left(\frac{\mathrm{K_{SO_4^{2-}}}}{\mathrm{K_{SO_4^{2-}}}+[\mathrm{SO_4^{2-}}]}\right)\left(\frac{\mathrm{K_{Fe(OH)_3^\alpha}}}{\mathrm{K_{Fe(OH)_3^\alpha}}+[\mathrm{Fe(OH)_3^\alpha}]}\right)\left(\frac{\mathrm{K_{NO_3^-}}}{\mathrm{K_{NO_3^-}}+[\mathrm{NO_3^-}]}\right)\left(\frac{\mathrm{K_{O_2}}}{\mathrm{K_{O_2}}+[\mathrm{O_2}]}\right)$	(E5)
$R_6 = k_1\mathrm{DIC}\left(\frac{\mathrm{K_{SO_4^{2-}}}}{\mathrm{K_{SO_4^{2-}}}+[\mathrm{SO_4^{2-}}]}\right)\left(\frac{\mathrm{K_{Fe(OH)_3^\alpha}}}{\mathrm{K_{Fe(OH)_3^\alpha}}+[\mathrm{Fe(OH)_3^\alpha}]}\right)\left(\frac{\mathrm{K_{NO_3^-}}}{\mathrm{K_{NO_3^-}}+[\mathrm{NO_3^-}]}\right)\left(\frac{\mathrm{K_{O_2}}}{\mathrm{K_{O_2}}+[\mathrm{O_2}]}\right)$	(E6)
Secondary redox and other reaction equations	
$R_7 = k_2[\mathrm{O_2}]\mathrm{NH_4^+}]$	(E7)
$R_8 = k_3[\mathrm{O_2}]\mathrm{Fe^{2+}}]$	(E8)
$R_9 = k_4\left[\mathrm{O_2}\right][\mathrm{FeS}]$	(E9)
$R_{10} = k_5[\mathrm{O_2}][\mathrm{FeS_2}]$	(E10)
$R_{11} = k_6\left[\mathrm{O_2}\right][\sum \mathrm{H_2}S]$	(E11)
$R_{12} = k_7\left[\mathrm{O_2}\right][\mathrm{CH_4}]$	(E12)
$R_{13} = k_8[\mathrm{Fe(OH)_3^\alpha}][\sum \mathrm{H_2}S]$	(E13)
$R_{14} = k_9[\mathrm{Fe(OH)_3^\beta}][\sum \mathrm{H_2}S]$	(E14)
$R_{15} = k_{10}[\mathrm{Fe^{2+}}][\sum \mathrm{H_2}S]$	(E15)
$R_{16} = k_{11}[\mathrm{FeS}][\sum \mathrm{H_2}S]$	(E16)
$R_{17} = k_{12}[S_0]$	(E17)
$R_{18} = k_{13}[\mathrm{FeS}][S_0]$	(E18)
$R_{19} = k_{14}[\mathrm{SO_4^{2-}}][\mathrm{CH_4}]$	(E19)
$R_{20} = k_{15}[\mathrm{Fe(OH)_3^{\alpha,\beta}}][\mathrm{CH_4}]$	(E20)
$R_{21} = k_{16}[\mathrm{Fe(OH)_3^\alpha}]$	(E21)
$R_{22} = k_{17}[\mathrm{Fe(OH)_3^\beta}]$	(E22)
$R_{23} = k_{18}\left[\mathrm{Fe^{2+}}\right][\mathrm{HPO_4^{2-}}]$	(E23)
$R_{24} = k_{19}\left[\mathrm{Fe^{2+}}\right][\mathrm{DIC}]$	(E24)
$R_{25} = k_{20}\left[\mathrm{FeCO_3}\right][\sum \mathrm{H_2}S]$	(E25)
$R_{26} = k_{21}\left[\mathrm{Fe_3(PO_4)_2}\right][\sum \mathrm{H_2}S]$	(E26)

(Soetaert and Meysman, 2012) to calculate the transport in porous media. The set of ordinary differential equations was subsequently solved numerically with the lsoda integrator algorithm (Hindmarsh, 1983; Petzoldt, 1983).

2.4.2 Transient scenario

The model applied in this study simulates the sediment deposition during the last 25000 years. A constant mass accumulation rate of $0.06\,\mathrm{g\,cm^{-2}\,yr^{-1}}$ over the Holocene was assumed. In order to reduce the computing time for the freshwater period, a higher mass accumulation rate of $1\,\mathrm{g\,cm^{-2}\,yr^{-1}}$ was used between 25 000 and 10 000 years before present (B.P.) and all fluxes were corrected accordingly (i.e., multiplied by a factor of 16.67). Inflow of Mediterranean saltwater into the Black Sea basin was modeled assuming an initial salinity of 1 for the freshwater lake and a linear increase to a salinity of 22 between 8500 and 1500 years B.P. (Fig. 2). Such a salinization scenario results in a good fit to the chloride ($\mathrm{Cl^-}$) profile (Fig. 3) and compares well with a previous salinity reconstruction, suggesting a linear increase in salinity of 1 to 22 between 9000 ± 500 years B.P. and 2000 ± 500 years B.P. (Soulet et al., 2010). Bottom water salinity was converted to $\mathrm{Cl^-}$ and $\mathrm{SO_4^{2-}}$ us-

Table 5. Reaction parameters used in the diagenetic model.

Parameter	Symbol	Value	Units	Values given in literature
Decay constant for OM^{α}	k_{α}	0.05	yr^{-1}	0.05–1.62[a,b]
Decay constant for OM^{β}	k_{β}	0.0086	yr^{-1}	0.0086[b]
Limiting concentration of O_2	K_{O_2}	0.02	mM	0.001–0.03[c]
Limiting concentration of NO_3^-	K_{NO_3}-	0.004	mM	0.004–0.08[c]
Limiting concentration of $Fe(OH)_3$	$K_{Fe(OH)_3}$	65	$\mu mol\,g^{-1}$	65–100[c]
Limiting concentration of SO_4^{2-}	$K_{SO_4^{2-}}$	1.6	mM	1.6[c]
Attenuation factor for SO_4^{2-} and methanogenesis	Ψ	0.0042	–	0.00157–0.075[b,d]
Rate constant for reaction E6	k_1	0.0011	yr^{-1}	
Rate constant for reaction E7	k_2	10 000	$mM^{-1}\,yr^{-1}$	5000–39 000[c,d]
Rate constant for reaction E8	k_3	140 000	$mM^{-1}\,yr^{-1}$	140 000[c]
Rate constant for reaction E9	k_4	300	$mM^{-1}\,yr^{-1}$	300[c]
Rate constant for reaction E10	k_5	1	$mM^{-1}\,yr^{-1}$	1[c]
Rate constant for reaction E11	k_6	160	$mM^{-1}\,yr^{-1}$	$\geq$ 160[c]
Rate constant for reaction E12	k_7	10 000 000	$mM^{-1}\,yr^{-1}$	10 000 000[c]
Rate constant for reaction E13	k_8	9.5	$mM^{-1}\,yr^{-1}$	$\leq$ 100[c]
Rate constant for reaction E14	k_9	0.95	$mM^{-1}\,yr^{-1}$	Model constrained
Rate constant for reaction E15	k_{10}	150	$mM^{-1}\,yr^{-1}$	100–14 800[b, d]
Rate constant for reaction E16	k_{11}	0.0003	$mM^{-1}\,yr^{-1}$	3.15[e]
Rate constant for reaction E17	k_{12}	3	yr^{-1}	3[f]
Rate constant for reaction E18	k_{13}	1	$mM^{-1}\,yr^{-1}$	7[f]
Rate constant for reaction E19	k_{14}	0.14	$mM^{-1}\,yr^{-1}$	10[c]
Rate constant for reaction E20	k_{15}	0.00000016	$mM^{-1}\,yr^{-1}$	0.0074[g]
Rate constant for reaction E21	k_{16}	0.6	yr^{-1}	0.6[f]
Rate constant for reaction E22	k_{17}	0.000013	yr^{-1}	Model constrained
Rate constant for reaction E23	k_{18}	0.052	$mM^{-1}\,yr^{-1}$	Model constrained
Rate constant for reaction E24	k_{19}	0.0027	$mM^{-1}\,yr^{-1}$	Model constrained
Rate constant for reaction E25	k_{20}	0.0008	$mM^{-1}\,yr^{-1}$	Model constrained
Rate constant for reaction E26	k_{21}	0.0008	$mM^{-1}\,yr^{-1}$	Model constrained

[a] Moodley et al. (2005). [b] Reed et al. (2011a). [c] Wang and Van Cappellen (1996). [d] Reed et al. (2011b). [e] Rickard and Luther (1997). [f] Berg et al. (2003). [g] Rooze et al. (2016).

ing the molecular weights and seawater density derived from the marelac geochemical dataset package (Soetaert et al., 2010; Table S1). A shift from oxic towards euxinic conditions around 7600 years B.P., with a peak in organic matter loading around 5300 years B.P. and constant elevated organic matter fluxes after 2700 years B.P. was assumed, following a recent study comprising data from seven sediment cores collected from the Black Sea (Eckert et al., 2013; Fig. 2). In addition, the input of organic matter was assumed to increase again in the last century, reflecting anthropogenic eutrophication of waters on the adjacent continental shelf as previously reported (Capet et al., 2013; Kemp et al., 2009). With the development of anoxic and sulfidic bottom water conditions, depositional fluxes of reactive Fe oxides were assumed to be zero (Fig. 2). In contrast, fluxes of Fe sulfides are high under euxinic conditions and dominated by FeS_2.

3 Results

3.1 Porewater profiles

Porewater profiles of SO_4^{2-} show a linear decrease from $\sim$ 17 mM at the sediment–water interface to a depth of $\sim$ 230 cm at both sites, below which CH_4 starts to accumulate in the porewater (Fig. 3). Bubble formation and degassing of CH_4 during gravity coring could not be avoided because of the high concentrations of CH_4 in the limnic deposits above the saturation of ca 1.3 mM CH_4 at atmospheric pressure (calculated for a salinity of 22 and a temperature of 25 °C using the algorithm from Mogollón et al., 2013). Observations of increased outgassing with depth during coring suggest that the low CH_4 concentrations in the deeper sediments at both sites are due to enhanced outgassing with increasing levels of CH_4. Porewater profiles of NH_4^+ at both sites are similar, and concentrations increase to $\sim$ 3 mM at depth, suggesting that actual CH_4 concentrations at both sites could be comparable. Most of the CH_4 values thus only in-

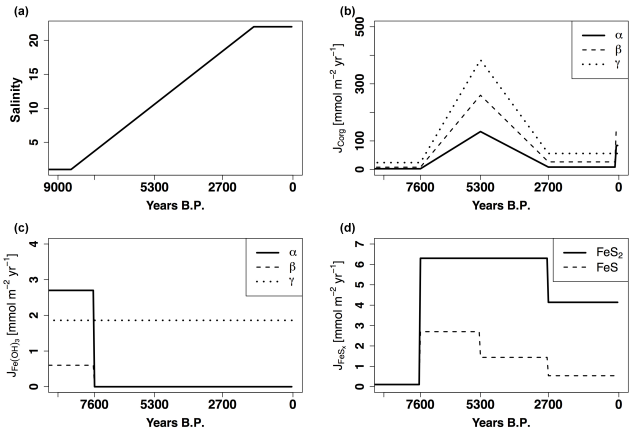

Figure 2. Transient evolution of salinity with a linear increase from 1 to 22 between 8500 and 1500 years B.P. **(a)**, fluxes of organic matter ($J_{C_{org}}$); **(b)** Fe oxides ($J_{Fe(OH)_3}$); **(c)** and Fe sulfides (J_{FeS_x}); **(d)** as implemented in the diagenetic model (site 4).

dicate the presence or absence of CH_4, and are not a quantitative measure (indicated as open diamonds in Fig. 4). Note that the upper ~ 300 cm of sediment at site 5 is likely less affected by CH_4 outgassing. Modeled porewater concentrations of CH_4, on the other hand, show a steep increase below the SMTZ, comparable to the gradient observed at site 5, and build up to concentrations of ~ 15 mM at depth (Fig. S5).

The SMTZ is located around 230 cm depth in the sediment and is characterized by the removal of both porewater SO_4^{2-} and dissolved CH_4. In this zone, SO_4-AOM drives the production of dissolved sulfide, DIC and alkalinity (Fig. S5) and diffusion of these porewater constituents away from the SMTZ (Fig. 3). Below the sulfide diffusion front, Fe^{2+} accumulates in the porewater. Dissolved HPO_4^{2-} reaches a maximum around the depth where sulfide levels drop below the detection limit of 1 µmol L^{-1}, followed by a steep decrease with depth. Concentrations of porewater Mn^{2+} are more than an order of magnitude lower than those of dissolved Fe^{2+}, and decrease from the sediment surface until ~ 200 cm depth, below which they slightly increase again (Fig. S5).

The smooth porewater profiles of $\delta^{13}C$–CH_4 and δD–CH_4 suggest that the isotopic composition of porewater CH_4 (available for site 5 only) is less affected by the CH_4 loss and reveals a biological origin in the limnic deposits, with hydrogenotrophic carbonate reduction, i.e., microbial reduction of CO_2 to CH_4 as the main methanogenic pathway for the range of CH_4 isotope ratios observed in these sediments (Fig. 4; Whiticar, 1999). Upward-diffusing CH_4 shows a gradual depletion in $\delta^{13}C$–CH_4 from ~ -74 at depth to ~ -96 ‰ around the SMTZ, followed by subsequent progressive ^{13}C enrichment towards the sediment surface. δD–CH_4 shows a small enrichment from -226 at depth to ~ -208 ‰ at the SMTZ and a strong shift towards high δD–CH_4 values of up to ~ 113 ‰.

3.2 Solid-phase profiles

A pronounced excursion in sedimentary C_{org} at site 4 in combination with a shift from gray clay deposits to microlaminated black sediments indicates that the lake–marine transition, i.e., the transition between the marine sapropel Unit II and the deep limnic sediments of Unit III (Arthur and Dean, 1998; Degens and Ross, 1974), is located around a sediment depth of ~ 90 cm at site 4 (Fig. 5). At site 5, Unit I and Unit II were lost due to a turbidite, explaining the low concentrations of C_{org} in the upper sediments.

Concentrations of solid S increase with decreasing depth from 20 µmol g^{-1} below 300 cm (sulfidization front) to ~ 400 µmol g^{-1} in the upper 100 cm at both sites and are dominated by FeS_2 (Fig. 5). Iron oxides show a decrease from ~ 100 µmol g^{-1} at depth to ~ 50 µmol g^{-1} in the sediments between 100 and 300 cm and a further decrease to ~ 10 µmol g^{-1} closer to the sediment surface. Amorphous Fe oxides (Fe_{ox1}) and more crystalline oxides (Fe_{ox2}) both account for half the total amount of Fe oxides, with a small contribution of recalcitrant oxides (Fe_{mag}; Fig. S4). The results from the two different Fe extractions applied in this study (Table 1) generally compare well (Fig. S4). Note, however, that the Fe oxides in Fig. 5 represent the results from the extraction after Poulton and Canfield (2005). Results from the Fe extractions modified from Claff et al. (2010) are provided in the Supplement. Sedimentary Mn content is relatively low at all three sites, ranging from ~ 5 to 10 µmol g^{-1} in the marine sediments to ~ 15 µmol g^{-1} in the deep limnic deposits of Unit III (Fig. S4).

Sediments below the sulfidization front are characterized by high Fe carbonate contents of ~ 100 µmol g^{-1}. The sharp depletion in Fe carbonate around the sulfidization front could only be reproduced in the model by assuming Fe carbonate dissolution by dissolved sulfide (Table 3). These results suggest a conversion of reactive Fe from carbonate toward sulfide phases in the presence of abundant dissolved sulfide.

Units I and II show high concentrations of organic P, which accounts for ~ 30 % of total P in these sediments (Fig. 5). Low organic P and high concentrations of detrital P in the upper sediments at site 5 are due to the turbidite. The limnic deposits of Unit III are generally depleted in organic P (< 6 % of total P) and enriched in detrital P. Authigenic Ca–P shows little variation in the sediments of Unit III, accounting for ~ 20 to 30 % of total P at the two sites. The contribution of Fe-associated P, on the other hand, is reduced in the limnic deposits of Unit III exposed to the downward-diffusing sulfide (~ 20 %) when compared to the sediments below the sulfidization front (~ 30 %). Concentrations of exchangeable P are < 2 µmol g^{-1} for sediments above the SMTZ and < 1 µmol g^{-1} for sediments at depth (data not shown).

Modeled SO_4^{2-} reduction rates (SRR) show two distinct peaks of ~ 200 pmol SO_4^{2-} cm^{-3} d^{-1} in the sediments of Unit II and in the sediments around the SMTZ (Fig. 6). Rates of CH_4 production are highest (~ 30 pmol CH_4 cm^{-3} d^{-1})

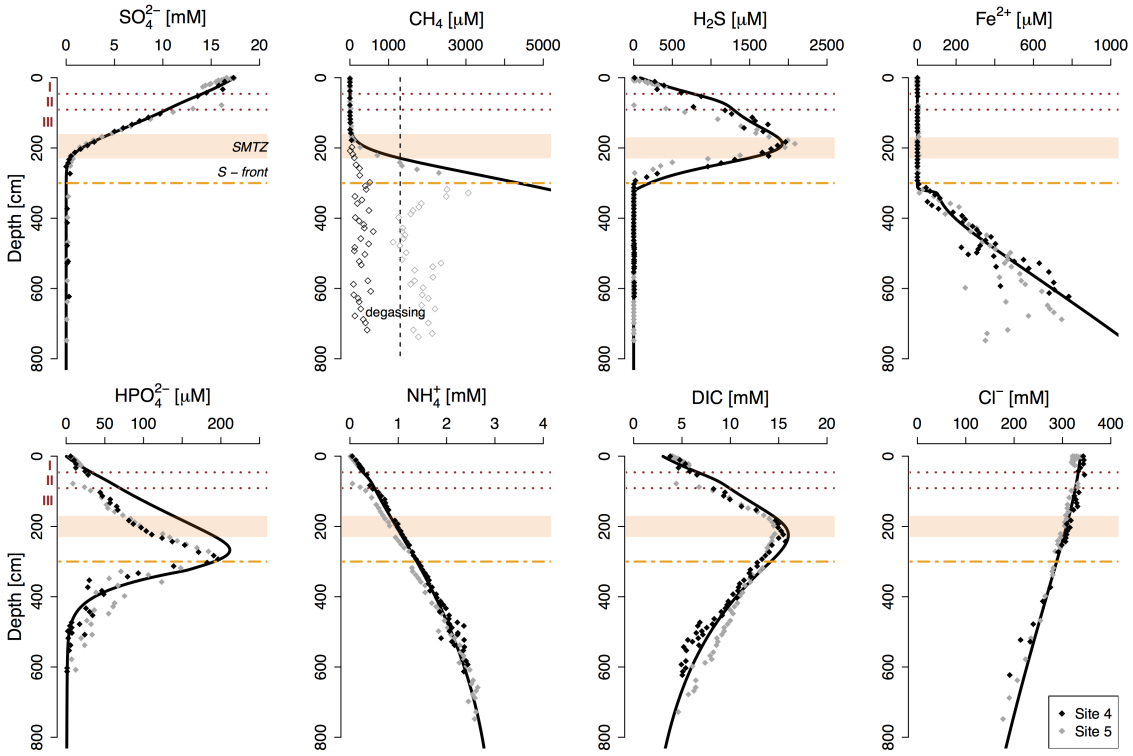

Figure 3. Porewater profiles of key components for site 4 (black diamonds) and site 5 (gray diamonds) and corresponding modeled profiles as calculated with the diagenetic model (black lines). Red dotted lines and roman numbers indicate the transitions between the lithological Unit I (modern coccolith ooze), Unit II (marine sapropel) and Unit III (limnic deposits). The orange bar represents the sulfate-methane transition zone (SMTZ), and the orange dashed line shows the current position of the downward-migrating sulfidization front (S front). The dashed vertical line indicates the CH_4 saturation concentration at atmospheric pressure (Mogollón et al., 2013). The open diamonds indicate CH_4 concentrations that are likely underestimated due to outgassing of CH_4 during coring.

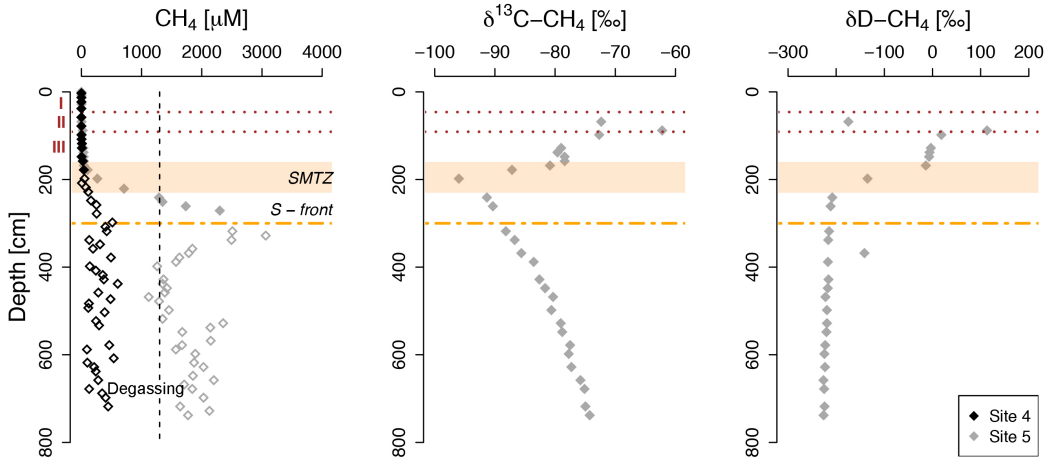

Figure 4. Porewater profiles of CH_4 for site 4 (black diamonds) and 5 (gray diamonds) and corresponding isotopic composition of dissolved CH_4 (available for site 5 only). $\delta^{13}C–CH_4$ values are given in ‰ vs. VPDB (Vienna Pee Dee Belemnite), and $\delta D–CH_4$ values are given in ‰ vs. V-SMOW (Vienna Standard Mean Ocean Water). Red dotted lines and roman numbers indicate the transitions between the lithological Unit I (modern coccolith ooze), Unit II (marine sapropel) and Unit III (limnic deposits). The orange bar represents the sulfate-methane transition zone (SMTZ), and the orange dashed line shows the current position of the downward-migrating sulfidization front (S front). The dashed vertical line indicates the CH_4 saturation concentration at atmospheric pressure (Mogollón et al., 2013). The open diamonds indicate CH_4 concentrations that are likely underestimated due to outgassing of CH_4 during coring.

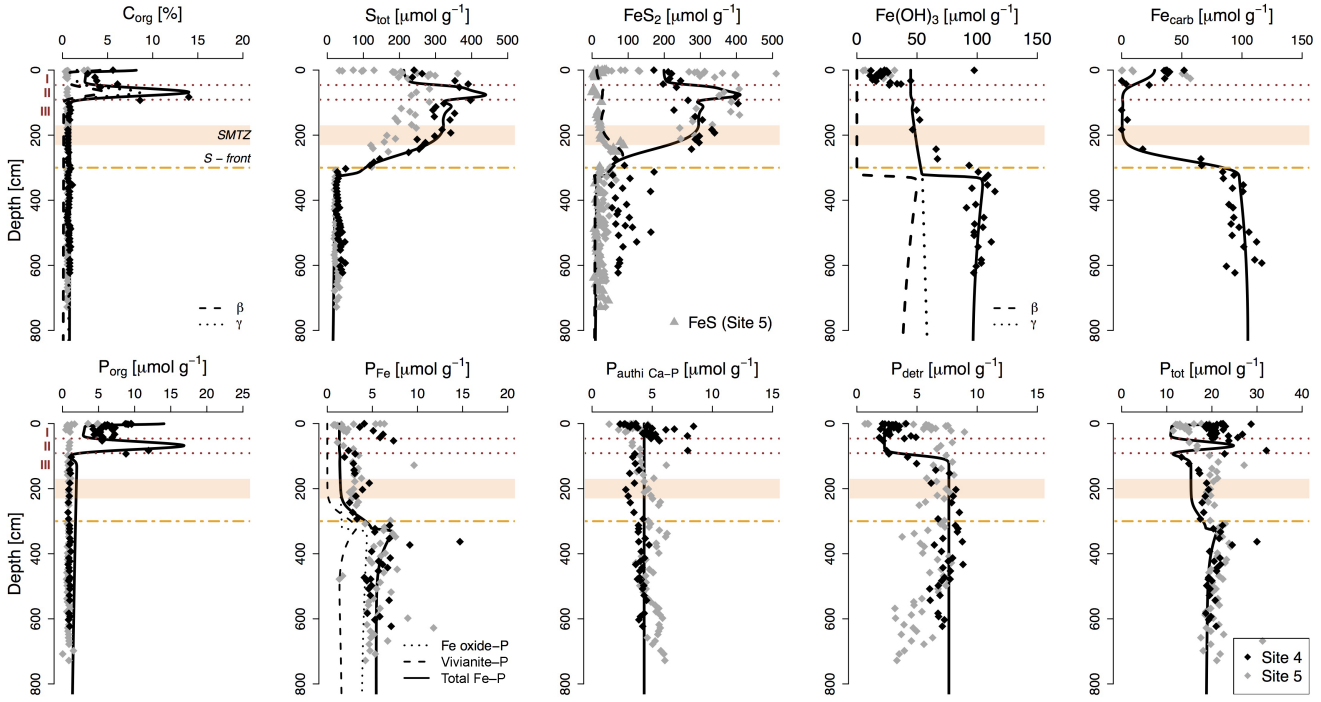

Figure 5. Solid-phase sediment profiles for site 4 (black diamonds) and 5 (gray diamonds). Fe oxides represent the sum of amorphous, crystalline and recalcitrant oxides, i.e., Fe_{ox1}, Fe_{ox2} and Fe_{mag} (Table 1, Fig. S4). Fe_{carb} was corrected for apparent AVS dissolution during the Na acetate extraction step (the uncorrected Fe_{carb} data are given in Fig. S4). Black lines represent profiles derived from the diagenetic model. Red dotted lines and roman numbers indicate the transitions between the lithological Unit I (modern coccolith ooze), Unit II (marine sapropel) and Unit III (limnic deposits). The orange bar represents the sulfate-methane transition zone (SMTZ), and the orange dashed line shows the current position of the downward-migrating sulfidization front (S front).

in the organic-rich marine deposits of Unit II and in the limnic deposits below the SMTZ. The sediments around the SMTZ are further characterized by high rates of SO_4-AOM ($\sim 200\,\mathrm{pmol\,cm^{-3}\,d^{-1}}$), whereas sediments directly below the sulfidization front show enhanced rates of S_0 disproportionation ($\sim 15\,\mathrm{pmol\,cm^{-3}\,d^{-1}}$). Organoclastic SO_4^{2-} reduction provides the main source for porewater sulfide in the organic-rich marine deposits, while SO_4-AOM and S_0 disproportionation are the dominant sources of dissolved sulfide in sediments around the SMTZ and directly below the sulfidization front, respectively. Rates of Fe-AOM are generally low ($< 0.04\,\mathrm{pmol\,CH_4\,cm^{-3}\,d^{-1}}$) and restricted to the limnic deposits only.

3.3 Temporal evolution

The temporal evolution in porewater and solid-phase constituents illustrates the impact of the lake–marine transition on the sediment geochemistry (Fig. 7). Concentrations of porewater Cl^- and SO_4^{2-} increase with the intrusion of marine Mediterranean Sea waters, accompanied by a decrease in dissolved CH_4 and accumulation of porewater sulfide in the shallower sediments. Dissolved Fe^{2+} becomes restricted to nonsulfidic porewaters at depth, while HPO_4^{2-} and solid S start to accumulate in the presence of dissolved sulfide. Iron oxides decrease in the surface sediments as well as in the sediments at depth. Vivianite, on the other hand, becomes increasingly enriched in sediments below the downward-diffusing sulfide front.

4 Discussion

4.1 Coupled S, CH_4 and Fe dynamics

4.1.1 Organoclastic SO_4^{2-} reduction

Model-derived areal rates of total SO_4^{2-} reduction of $\sim 0.24\,\mathrm{mmol\,SO_4^{2-}\,m^{-2}\,d^{-1}}$ (Table 6), i.e., the total amount of SO_4^{2-} reduced per square meter of sea floor, compare well with calculated diffusive fluxes of SO_4^{2-} into the sediment at sites 4 and 5 (~ 0.21 and $0.20\,\mathrm{mmol\,SO_4^{2-}\,m^{-2}\,d^{-1}}$, respectively) and are in good agreement with previous SO_4^{2-} flux estimates of 0.17 to $0.28\,\mathrm{mmol\,SO_4^{2-}\,m^{-2}\,d^{-1}}$ for sediments of the western Black Sea (Jørgensen et al., 2001). In the model, organoclastic SO_4^{2-} reduction accounts for > 65 % of total organic matter degradation in the upper 800 cm of sediment, supporting previous conclusions that SO_4^{2-} reduc-

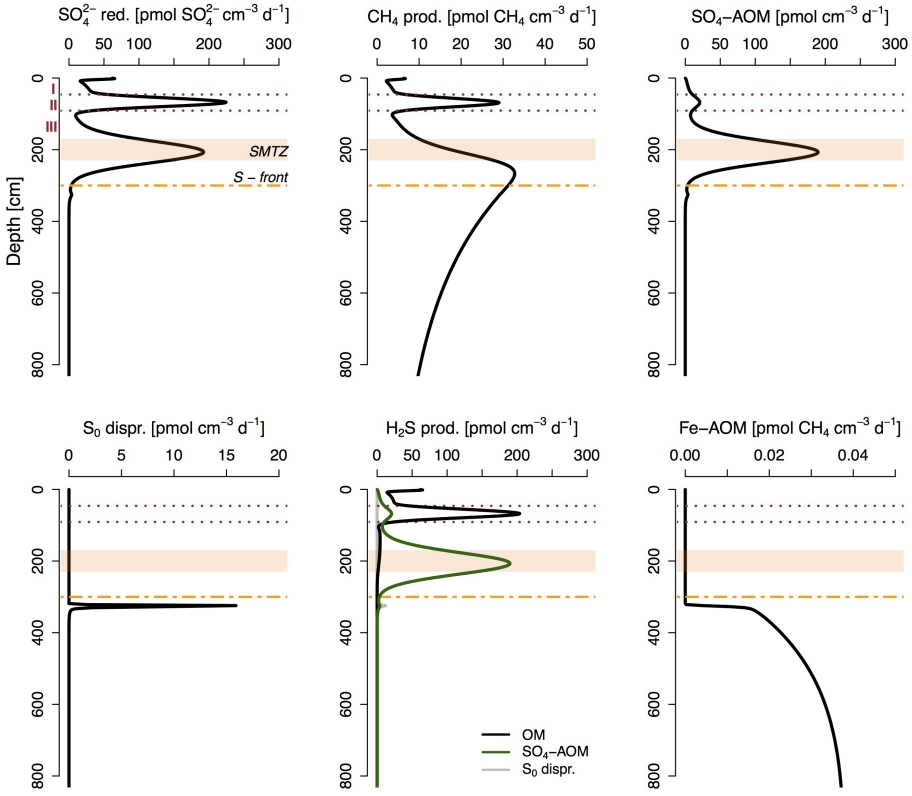

Figure 6. Modeled rates of total SO_4^{2-} reduction, total CH_4 production, SO_4-AOM, S_0 disproportionation, sulfide production and Fe-AOM. Red dotted lines and roman numbers indicate the transitions between the lithological Unit I (modern coccolith ooze), Unit II (marine sapropel) and Unit III (limnic deposits). The orange bar represents the sulfate-methane transition zone (SMTZ), and the orange dashed line shows the current position of the downward-migrating sulfidization front (S front).

Table 6. Depth-integrated rates of key processes for selected depth intervals in μmol m^{-2} d^{-1}.

Process	0–90 cm[a]	90–300 cm[b]	300–800 cm[c]	0–800 cm
Organoclastic SO_4^{2-} reduction[d]	68.9	5.3	0.003	74.2
CH_4 production[e,f]	10.21	37.7	91.8	139.8
SO_4 – AOM	9.4	151.6	1.2	162.2
Fe–AOM[e]	0	0	1.2	1.2
S_0 disproportionation	0	0	0.9	0.9

[a] Marine deposits. [b] Limnic sediments around the SMTZ with dissolved sulfide. [c] Nonsulfidic limnic deposits. [d] Per mol of SO_4^{2-}. [e] Per mol of CH_4. [f] Sum of CH_4 production from organic matter and from DIC (i.e., CO_2).

tion represents the dominant mineralization process of organic matter in sediments below the chemocline (Jørgensen et al., 2001; Thamdrup et al., 2000). The remaining < 25 % of organic matter remineralization is due to methanogenesis. The relative contribution of SO42-reduction to organic matter remineralization, however, is likely significantly higher when taking into account the high SRR in the uppermost sediment layers (Jørgensen et al., 2001), which are not captured by our model.

The depth-dependent rate profile of SO_4^{2-} reduction shows two distinct peaks of ∼ 70 and 230 pmol SO_4^{2-} cm^{-3} d^{-1} associated with organoclastic SO_4^{2-} reduction in the organic-matter-rich marine deposits of Unit I and Unit II. These rates are at the low end of reported values from Black Sea sediments (0.1–20 nmol cm^{-3} d^{-1}; Holmkvist et al., 2011b; Jørgensen et al., 2001, 2004; Knab et al., 2009; Leloup et al., 2007). Our model further demonstrates that the two SRR peaks in the sediments of Unit I and Unit II are not reflected in the porewater profile of SO_4^{2-}. This finding is in line with earlier work, showing that the SO_4^{2-} gradient in Black Sea sediments is primarily affected by SO_4-AOM in the SMTZ (Jørgensen et al., 2001). The shorter diffusion distance (the

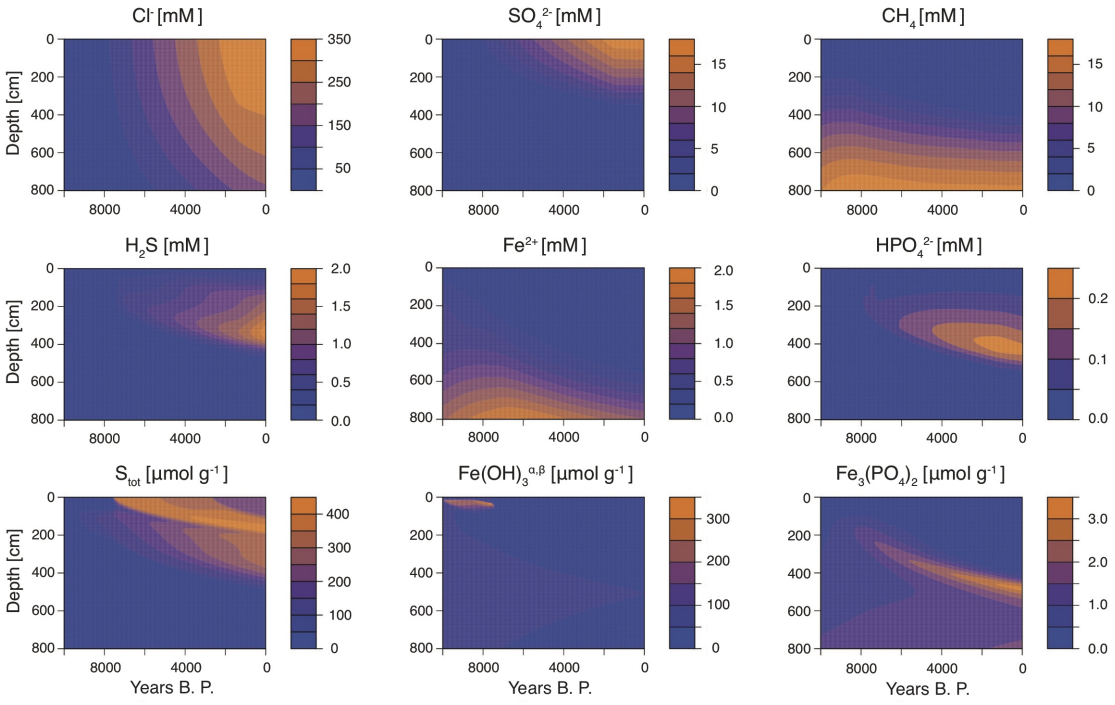

Figure 7. Transient evolution of selected porewater and sediment profiles with depth as calculated for site 4 using the diagenetic model.

diffusion time to ∼ 200 cm is about 5 times longer than to ∼ 90 cm, i.e., ∼ 300 years vs. ∼ 60 years) and higher porosity in Unit I and II (Fig. S1) both dampen the effect of SO_4^{2-} reduction in the marine deposits on the SO_4^{2-} profile (see also Jørgensen et al., 2001). Thus, our results support previous conclusions that SRR estimates based on porewater profiles of SO_4^{2-} (i.e., net SO_4^{2-} consumption) alone may underestimate the actual SO_4^{2-} turnover (i.e., gross SO_4^{2-} reduction) in marine sediments (Jørgensen, 1978; Jørgensen et al., 2001).

4.1.2 SO_4-AOM

Porewater profiles of SO_4^{2-}, CH_4, sulfide and DIC reveal a distinct SMTZ around 230 cm depth at both sites, where SO_4-AOM with upward-diffusing CH_4 results in the concomitant removal of porewater SO_4^{2-} and CH_4 and in the accumulation of dissolved sulfide and DIC in the porewaters of these sediments (Fig. 3). The depth of the SMTZ and the steep increase in CH_4 to > 3 mM below the SMTZ found in this study are consistent with earlier observations in sediments of the western Black Sea (Henkel et al., 2012; Holmkvist et al., 2011b; Jørgensen et al., 2001, 2004; Knab et al., 2009; Leloup et al., 2007). The location of the SMTZ, however, has progressed downwards in the last ca. 9000 years, following the inflow of SO_4^{2-}-rich saltwater into the Black Sea basin (Fig. 7; see also Henkel et al., 2012).

Calculated diffusive fluxes of SO_4^{2-} and CH_4 to the SMTZ (∼ 0.2 mmol SO_4^{2-} m^{-2} d^{-1} and 0.08 mmol CH_4 m^{-2} d^{-1}) and modeled areal rates of SO_4-AOM (∼ 0.16 mmol m^{-2} d^{-1}) suggest that AOM accounts for ∼ 40 to 70 % of the total SO_4^{2-} reduction in these sediments, with the remaining ∼ 30 to 60 % attributed to organoclastic SO_4^{2-} reduction. Such a high contribution of AOM exceeds the range of previous estimates that included experimentally measured SRR close to the sediment surface (∼ 7 to 18 %; Jørgensen et al., 2001, 2004). Around the SMTZ, SO_4-AOM is responsible for ∼ 97 % of the total SO_4^{2-} reduction (Fig. 6 and Table 6), thus enhancing the downward diffusive flux of sulfide into the deep limnic deposits of Unit III. Our model suggests that without this additional source of sulfide through SO_4-AOM, the sulfidization front would currently be located around 150 cm depth in the sediment (Fig. 8).

The consumption of upward-diffusing CH_4 by SO_4^{2-}-driven AOM leads to a progressive enrichment of ^{13}C and D in the residual CH_4 above the SMTZ (Fig. 4) due to the preferential oxidation of isotopically light CH_4 during SO_4-AOM (Alperin et al., 1988; Martens et al., 1999; Whiticar, 1999). Interestingly, porewater CH_4 above the SMTZ shows unusually high δD–CH_4 values that fall outside of the common range observed for porewater δD–CH_4 (e.g., Whiticar, 1999). Future studies, however, are needed to resolve the cause of the strong D enrichment of dissolved CH_4 above the SMTZ in Black Sea sediments.

Modeled concentrations of CH_4 indicate that the measurements above the sulfidization front at site 5 are likely less affected by outgassing during core recovery (Fig. 4)

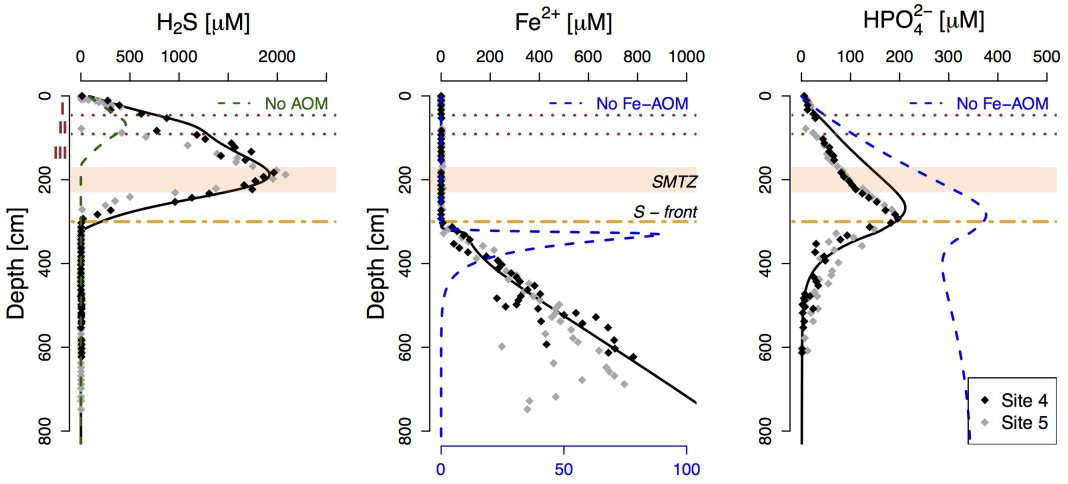

Figure 8. Porewater profiles of dissolved sulfide, Fe^{2+} and HPO_4^{2-}. The green dashed line represents the modeled sulfide profile without SO_4-AOM, indicating that the latter significantly enhances the downward sulfidization. Blue dashed lines denote the modeled Fe^{2+} and HPO_4^{2-} profiles without ongoing Fe oxide reduction in the limnic deposits (i.e., no Fe-AOM). Note that concentrations of Fe^{2+} were multiplied 10 times in the model simulation without Fe oxide reduction to better visualize the potential release of Fe^{2+} through a cryptic S cycle (corresponding x axis at bottom). Red dotted lines and roman numbers indicate the transitions between the lithological Unit I (modern coccolith ooze), Unit II (marine sapropel) and Unit III (limnic deposits). The orange bar represents the sulfate-methane transition zone (SMTZ), and the orange dashed line shows the current position of the downward-migrating sulfidization front (S front).

and can thus be used to derive kinetic isotope fractionation factors for carbon (ε_C) and hydrogen (ε_H) associated with SO_4-AOM at the SMTZ using the Rayleigh distillation function (Crowe et al., 2011; Egger et al., 2015b; Rayleigh, 1896; Whiticar, 1999). Corresponding estimates for ε_C of $\sim 8\,‰$ ($R^2 = 0.972$) and ε_H of $\sim 58\,‰$ ($R^2 = 0.982$) are at the lower end of previously documented values in marine and brackish–marine environments (8–38 ‰ for ε_C and 100–324 ‰ for ε_H; Alperin et al., 1988; Egger et al., 2015b; Holler et al., 2009; Martens et al., 1999; Reeburgh, 2007). Note, however, that the Rayleigh distillation function only applies to closed systems (Rayleigh, 1896). These estimates should therefore be interpreted as an approximation, as more accurate estimates would require isotope modeling (e.g., Alperin et al., 1988).

At the base of the SMTZ, upward-diffusing CH_4 reveals an initial depletion in $\delta^{13}C$–CH_4 (Fig. 4). Such a shift to ^{13}C-depleted CH_4, together with a decrease in its concentration, could indicate an enzyme-mediated equilibrium C isotope exchange during SO_4-AOM at low SO_4^{2-} concentrations (< 0.5 mM; Holler et al., 2012; Yoshinaga et al., 2014). The effect of such mechanisms on deuterated CH_4 is likely limited.

4.1.3 Cryptic S cycling

Earlier studies showed evidence for ongoing SO_4^{2-} reduction (< 1 nmol cm^{-3} d^{-1}) within the SO_4^{2-}-depleted (< 0.5 mM) limnic deposits below the SMTZ in sediments of the Black Sea (Holmkvist et al., 2011b; Knab et al., 2009; Leloup et al., 2007), Baltic Sea (Holmkvist et al., 2011a, 2014; Leloup et al., 2009) and Alaskan Beaufort Sea (Treude et al., 2014), likely driven by SO_4^{2-} production from re-oxidation of dissolved sulfide with oxidized Fe minerals. In this mechanism, Fe oxides enhance the recycling of sulfide to SO_4^{2-} in a cryptic S cycle (Holmkvist et al., 2011a; Treude et al., 2014), thereby fueling SO_4^{2-}-driven AOM in Fe-oxide-rich sediments. In this cryptic S cycle, dissolved sulfide is oxidized to zerovalent sulfur (S_0), a key intermediate in AOM, which is subsequently disproportionated to SO_4^{2-} and sulfide by associated *Deltaproteobacteria* (Holmkvist et al., 2011a; Milucka et al., 2012; Sivan et al., 2014; Treude et al., 2014). The additional SO_4^{2-}, produced during S_0 disproportionation, may then be re-used by the methanotrophic archaea as an electron acceptor for SO_4-AOM (Milucka et al., 2012).

Our model results suggest slow rates of ongoing SO_4^{2-} reduction of < 0.2 nmol cm^{-3} d^{-1} (Fig. 6) within the limnic deposits below the SMTZ exposed to dissolved sulfide (Table 6), in line with estimated SRR based on $^{35}SO_4^{2-}$ incubation experiments with Black Sea sediments from below the SMTZ of $\sim$ 0.1–0.5 nmol cm^{-3} d^{-1} (Knab et al., 2009; Leloup et al., 2007). Below the sulfidization front, SRR show a distinct peak of $\sim$ 5 pmol cm^{-3} d^{-1}. Active SO_4^{2-} reduction in these SO_4^{2-}-depleted sediments requires deep SO_4^{2-} formation to maintain low net rates of SO_4^{2-} reduction. In the model, S_0 disproportionation is the only potential source of porewater SO_4^{2-} at depth (Table 3). Formation of S_0, in turn, occurs exclusively by oxidation of dissolved sulfide during the reductive dissolution of Fe oxides, explaining the distinct

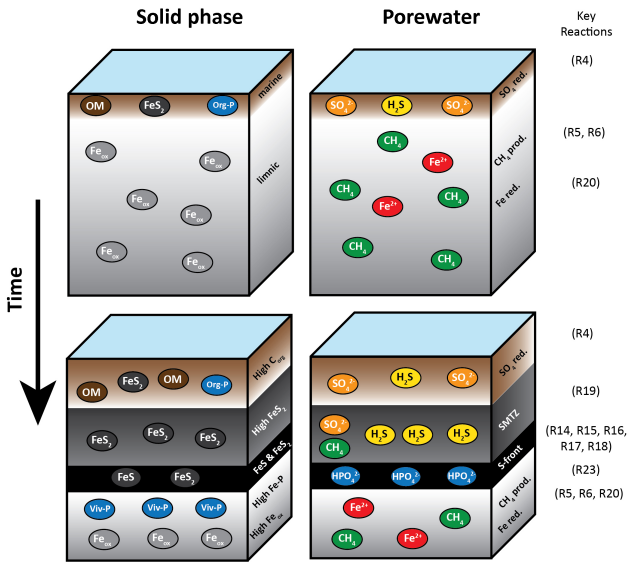

Figure 9. Schematic of the main diagenetic processes discussed in this study and their imprint on the geochemical solid-phase (left) and porewater profiles (right). Accumulation of marine sediments with time and the subsequent downward diffusion of SO_4^{2-} into the CH_4-bearing limnic sediment stimulate SO_4-AOM around the sulfate-methane transition zone (SMTZ), thus enhancing the downward sulfidization of the Fe-oxide-rich lake deposits. Below the sulfidization front (S front), HPO_4^{2-} released during reductive dissolution of Fe oxides is bound again in vivianite, leading to an enrichment in sedimentary P in these sediments. Numbers on the right indicate the key reactions occurring in the corresponding sediment layers as described in Table 3. Note that in this study, Fe-AOM (R20) was assumed as the main source of porewater Fe^{2+} below the S front to further test the potential impact of Fe-AOM on porewater CH_4. However, based on the geochemical data, we cannot exclude a potential role for organoclastic Fe reduction (R3) and/or reactivation of less reactive Fe oxides by methanogens.

S_0 disproportionation peak of $\sim 15\,\mathrm{pmol\,cm^{-3}\,d^{-1}}$ around the sulfidization front (Fig. 6). Thus, based on the model assumptions, we conclude that Fe oxides increase the transformation of sulfide to SO_4^{2-} via formation and subsequent disproportionation of S_0 in these sediments, as suggested previously (Holmkvist et al., 2011b; Knab et al., 2009; Leloup et al., 2007). Such recycling of SO_4^{2-} stimulates slow rates of SO_4-AOM in the sediments below the SMTZ, explaining the low background rates of SO_4^{2-} reduction in the SO_4^{2-}-depleted limnic deposits. These results support recent findings of indirect Fe-stimulated SO_4^{2-}-driven AOM in laboratory experiments (Sivan et al., 2014), and highlight that Fe oxides could play a significant role as stimulators of AOM and S recycling in natural environments.

4.2 Fe reduction below the sulfidization front

Below the sulfidization front, Fe^{2+} starts to accumulate in the porewater (Fig. 3). Although previous studies have also reported an increase of dissolved Fe^{2+} around the depth where sulfide levels drop below the detection limit (Holmkvist et al., 2011b; Jørgensen et al., 2004; Knab et al., 2009), the source of this porewater Fe^{2+} has remained unknown. One possible explanation could be that the elevated Fe^{2+} concentrations at depth represent remnant Fe^{2+} accumulated during the Black Sea "lake" phase (Knab et al., 2009). In our model, Fe^{2+} shows a broad peak of $\sim 300\,\mu M$ until $\sim 300\,cm$ depth in the sediment during the initial lake phase, assuming organoclastic Fe reduction to be the only Fe reduction pathway (data not shown). The removal of Fe^{2+} through authigenic formation of reduced Fe(II) minerals, however, prevents the accumulation of substantial amounts of Fe^{2+} in the porewater below $\sim 300\,cm$ sediment depth during the lake phase (Fig. 8). We therefore conclude that the high concentrations of dissolved Fe^{2+} below the sulfidization front are most likely indicative of active Fe reduction in these sediments.

4.2.1 Fe reduction through cryptic S cycling

In theory, a cryptic S cycle, as described in Sect. 4.1.3, could result in net accumulation of dissolved Fe^{2+} if the sulfide consumption from reaction with ferric Fe outweighs the production of sulfide from SO_4^{2-} reduction. Modeled Fe^{2+} indeed shows a peak of $< 100\,\mu M$ directly below the sulfidization front, assuming no active Fe reduction in the limnic deposits (Fig. 8). Model simulations further indicate that, based on the reaction network used in this study (Table 3), cryptic S cycling could result in a buildup of porewater Fe^{2+} of $\sim 300\,\mu M$ at depth in the sediment provided there was no precipitation of reduced Fe(II) minerals (Fig. S2). However, concentrations of dissolved Fe^{2+} are too low compared to the measurements and are confined to sediments between 300 and 400 cm depths only. The diagenetic model developed in this study therefore suggests that cryptic S cycling is unlikely to explain the high concentrations ($\sim 800\,\mu M$) of dissolved Fe^{2+} observed in the deep limnic deposits.

4.2.2 Organoclastic Fe reduction

In the model, the reduction of Fe oxides coupled to organic matter degradation only occurs with the easily reducible α phase in order to allow for the burial of the more crystalline β phase at depth (Table 3). Since the α phase is efficiently reduced in the upper few centimeters during organoclastic Fe reduction, no easily reducible Fe oxides are being buried into the deep sediments in the diagenetic model. Organoclastic Fe reduction therefore does not occur within the modeled deep limnic deposits that exclusively contain more crystalline (β) and refractory (γ) Fe oxides (Fig. 5). Instead, we assume that CH_4 represents a plausible electron donor for the reduction of more crystalline Fe oxides in the organic-poor deep sediments with relatively refractory old organic matter ($< 0.8\,wt\,\%$). The exclusion of organoclastic Fe reduction at

depth in the model provides an estimate of an upper constraint on the potential importance of Fe-AOM in Black Sea sediments. As a result of this assumption, however, the model results cannot be used to conclude whether Fe-AOM is more likely than organoclastic Fe reduction.

An increasing body of geochemical evidence and laboratory incubation experiments shows that Fe-AOM might be occurring in a variety of different aquatic environments (Amos et al., 2012; Beal et al., 2009; Crowe et al., 2011; Egger et al., 2015b; Riedinger et al., 2014; Scheller et al., 2016; Segarra et al., 2013; Sivan et al., 2011; Wankel et al., 2012). In addition, several studies have shown that Fe-reducing microorganisms are able to outcompete methanogens for common substrates (e.g., acetate and H_2), thus reducing the concentrations of these common primary electron donors to levels that are too low for methanogens to grow (Achtnich et al., 1995; Lovley and Phillips, 1987; Lovley et al., 1989). These results, together with the observed capability of methanogens to switch from CH_4 production to Fe reduction (Bodegom et al., 2004; Bond and Lovley, 2002; Liu et al., 2011; Reiche et al., 2008; Sivan et al., 2016; Vargas et al., 1998), led to the common conclusion that Fe oxides exert a suppressive effect on methanogenesis. Ongoing CH_4 production in the Fe-oxide-rich limnic deposits, as deduced from the isotopic composition of porewater CH_4 (Fig. 4), could then indicate limited organoclastic Fe reduction in these sediments.

However, there is increasing evidence that (semi)conductive crystalline Fe oxides (e.g., hematite and magnetite) can, in fact, stimulate concurrent methanogenesis and organoclastic Fe reduction through direct interspecies electron transfer, by serving as electron conduits among syntrophic CH_4-producing organisms at rates that are substantially higher than those for interspecies electron transfer by H_2 (Cruz Viggi et al., 2014; Kato et al., 2012; Li et al., 2014; Zhou et al., 2014; Zhuang et al., 2015). The inhibitory effect of Fe reduction on methanogenesis thus appears to be lower for crystalline Fe oxides such as hematite and magnetite, which are less bioavailable to Fe-reducing organisms than poorly crystalline (amorphous) Fe oxides (e.g., ferrihydrite and lepidocrocite; Lovley, 1991; Qu et al., 2004; Zhuang et al., 2015). These findings indicate that the crystallinity and conductivity of Fe oxides may play a key role in determining whether methanogenesis is stimulated or suppressed in Fe-oxide-rich environments. In addition, the presence of methanogens that are able to rapidly switch between methanogenesis and reduction of Fe oxides could also result in a reactivation of less reactive Fe oxides that were not reduced during initial organoclastic Fe reduction in the deep methanogenic zone as suggested by Sivan et al. (2016). Thus, the deep limnic sediments may be characterized by a complex interplay of concurrent methanogenesis, Fe oxide reduction and methanotrophy, i.e., AOM.

4.2.3 Fe-AOM

Our model results indicate that Fe-AOM could also be a possible mechanism explaining the buildup of porewater Fe^{2+} below the sulfidization front. Previous studies have shown that in systems where production and oxidation of CH_4 take place concurrently, methanogenesis might conceal the isotopic signature of AOM (Egger et al., 2015b; Seifert et al., 2006; Whiticar, 1999). Thus, unlike SO_4-AOM, Fe-dependent AOM likely only has little effect on the isotopic composition of porewater CH_4 due to the removal of small amounts of CH_4 in sediments with ongoing methanogenesis. This might explain why porewater CH_4 does not show enrichment in both heavy isotopes below the sulfidization front as would be expected if Fe-AOM would occur, but rather indicates antipathetic changes, i.e., depletion in ^{13}C–CH_4 and enrichment in D–CH_4, usually attributed to CH_4 production from carbonate reduction (Chanton et al., 2005; Whiticar, 1999).

Model-derived rates for Fe-AOM of $\sim 0.04\,\mathrm{pmol\,cm^{-3}\,d^{-1}}$ (Fig. 6) are significantly lower than potential Fe-AOM rates of $\sim 4\,\mathrm{nmol\,cm^{-3}\,d^{-1}}$ estimated from laboratory incubation studies (Egger et al., 2015b; Segarra et al., 2013; Sivan et al., 2011) with brackish and limnic sediment samples. This large deviation is likely due to an overestimation of Fe-AOM rates derived from stimulated microbial communities under laboratory conditions using freshly synthesized and thus easily bioavailable Fe oxides when compared to in situ conditions.

In the upper 800 cm of sediment, Fe-AOM accounts for $< 1\,\%$ of total CH_4 oxidation, with the remaining $> 99\,\%$ attributed to SO_4-AOM (Table 6; see also Fig. S2). However, while high rates of SO_4-AOM are mainly restricted to the SMTZ, Fe-AOM might occur over a deep methanogenic zone, reaching far down into the sediment. To accurately assess the contribution of Fe-AOM to the total CH_4 consumption in Black Sea sediments, additional knowledge about the vertical expansion of the Fe-oxide-rich limnic sediments deposited during the Blake Sea lake phase would be required.

4.3 Impact of S–Fe–CH_4 dynamics on sedimentary P diagenesis

Degradation of organic matter and the subsequent release of HPO_4^{2-} to the porewater during early diagenesis typically results in a sink-switching from organic P to authigenic P-bearing phases such as Ca phosphates (Filippelli, 1997; Ruttenberg and Berner, 1993; Slomp et al., 1996b), Mn–Ca carbonates (Jilbert and Slomp, 2013; Mort et al., 2010; Suess, 1979) or reduced Fe phosphates (Burns, 1997; Jilbert and Slomp, 2013; Martens et al., 1978; März et al., 2008). Reductive dissolution of Fe oxides by dissolved sulfide and the following liberation of HPO_4^{2-} may also contribute to the buildup of porewater HPO_4^{2-} (Burns, 1997; Egger et al., 2015a; März et al., 2008; Schulz et al., 1994). Thus, the

downward sulfidization ultimately results in the accumulation of dissolved HPO_4^{2-} in the porewater as the sulfidization front moves downward into the limnic deposits (Fig. 7).

The porewater profile of HPO_4^{2-} (Fig. 3) indicates the presence of a sink for HPO_4^{2-} below the sulfidization front and, to a lesser extent, in the sulfidic sediments around the SMTZ, likely unrelated to Ca–P authigenesis (Fig. 5). Such a sink for HPO_4^{2-} below sulfidic sediments has been observed previously (Burns, 1997; Egger et al., 2015a; März et al., 2008; Schulz et al., 1994; Slomp et al., 2013) and shown to be most likely the result of vivianite formation (Egger et al., 2015a; Hsu et al., 2014; März et al., 2008). Abundant dissolved Fe^{2+} and a peak in Fe-associated P below the sulfidization front observed in this study (Figs. 3 and 5) suggest that vivianite authigenesis might also be occurring in the limnic deposits below the sulfidization front in Black Sea sediments.

Assuming that vivianite formation represents the only sink for porewater HPO_4^{2-} results in a good fit between the modeled and measured porewater profile of HPO_4^{2-} below the sulfidization front (Fig. 3). Modeled vivianite formation accounts for up to 70 % of total Fe-associated P directly below the sulfidization front. However, the model underestimates the sharp peak in Fe-associated P directly below the sulfidization front, suggesting that modeled vivianite formation likely underestimates the actual contribution of vivianite in these sediments. In the limnic deposits not yet impacted by the downward sulfidization, modeled vivianite accounts for $\sim$ 20–30 % of total Fe-associated P. From this, we estimate that vivianite may be responsible for > 20 % of total P burial directly below the sulfidization front and for $\sim$ 10 % of total P burial in the deep limnic deposits at depth.

Running the model without Fe-AOM and thus without Fe reduction at depth results in modeled porewater HPO_4^{2-} concentrations of up to $\sim$ 350 µM at depth in the sediment (Fig. 8). This suggests that Fe-AOM can promote conditions that allow sequestration of a significant proportion of P as vivianite in the limnic deposits below the sulfidization front. Consistent with earlier findings, Fe-AOM likely only accounts for a small fraction of total CH_4 oxidation, but may substantially impact the biogeochemical cycling of sedimentary P (Egger et al., 2015a, b; Rooze et al., 2016).

The deviation between the modeled and measured profiles of HPO_4^{2-} and Fe-associated P in the upper 300 cm of sediment (Figs. 3 and 5) could indicate apatite authigenesis (Dijkstra et al., 2014) or the formation of vivianite in microenvironments as previously suggested for sulfidic sediments (Dijkstra et al., 2014; Jilbert and Slomp, 2013). For example, *Deltaproteobacteria*, known to be involved in SO_4-AOM, have been shown to accumulate Fe- and P-rich inclusions in their cells (Milucka et al., 2012). They may therefore provide a potential explanation for the occurrence of Fe-associated P in sulfidic sediments (Dijkstra et al., 2014; Jilbert and Slomp, 2013). However, such microenvironments are not captured in our model.

In the diagenetic model, vivianite undergoes dissolution if sulfide is present in the porewaters (Table 3). Sulfide-induced vivianite dissolution significantly improved the model fit to the measured HPO_4^2 and sulfide data. With the downward migration of dissolved sulfide, modeled vivianite becomes increasingly enriched below the sulfidization front (Fig. 7). Thus, similar to the sulfidization front, a downward diffusive vivianite front may exist in sedimentary systems experiencing downward sulfidization.

In summary, the enhanced downward sulfidization driven by SO_4-AOM leads to dissolution of Fe oxide-bound P in the lake deposits. Below the sulfidization front, downward-diffusing HPO_4^{2-} is bound again in authigenic vivianite due to high concentrations of dissolved Fe^{2+} at depth in the sediment generated by ongoing Fe oxide reduction. As a result, trends in total P with depth are significantly altered, showing an accumulation in total P below the sulfidization front unrelated to changes in organic matter deposition and enhanced sedimentary P burial during deposition.

5 Conclusions

In the Black Sea, the shift from a freshwater lake to a marine system and subsequent downward diffusion of marine SO_4^{2-} into the CH_4-bearing lake sediments results in a multitude of diagenetic reactions around the SMTZ (Fig. 9). The diagenetic model developed in this study shows that SO_4-AOM within the SMTZ significantly enhances the downward diffusive flux of sulfide into the deep limnic deposits, forming a distinct diagenetic sulfidization front around 300 cm depth in the sediment. Our results indicate that without this additional source of dissolved sulfide in the SMTZ, the current sulfidization front would be located around a depth of 150 cm. During the downward sulfidization, Fe oxides, Fe carbonates and vivianite are converted to Fe sulfide phases, leading to an enrichment in solid-phase S contents and the release of HPO_4^{2-} to the porewater. Our results further support the hypothesis that part of the downward-migrating sulfide is re-oxidized to SO_4^{2-} upon reaction with ferric Fe minerals, fueling a cryptic S cycle and thus stimulating slow rates ($\sim$ 1–100 pmol cm^{-3} d^{-1}) of SO_4-AOM in the SO_4^{2-}-depleted limnic deposits below the SMTZ (Holmkvist et al., 2011a, b; Knab et al., 2009; Leloup et al., 2007).

We propose that besides organoclastic Fe oxide reduction and reactivation of less reactive Fe oxides by methanogens, AOM coupled to the reduction of Fe oxides may also be a possible mechanism explaining the high concentrations of Fe^{2+} in the porewater below the sulfidization front. The buildup of dissolved Fe^{2+} at depth creates conditions that allow sequestration of the downward-diffusing HPO_4^{2-} as authigenic vivianite, resulting in an accumulation of total P in these sediments.

The diagenetic processes described here reveal that AOM may strongly overprint burial records of Fe, S and P in depositional marine systems subject to changes in organic matter loading or water column salinity such as coastal environments (Egger et al., 2015a; Rooze et al., 2016), deep-sea fan sediments (März et al., 2008; Schulz et al., 1994) and many high-latitude seas (Holmkvist et al., 2014; Treude et al., 2014). Interpreting these diagenetic patterns as primary sedimentary signals may lead to incorrect reconstructions of environmental conditions during sediment deposition.

6 Data availability

All data files are available from the PANGAEA database (https://doi.org/10.1594/PANGAEA.864617).

The Supplement related to this article is available online at doi:10.5194/bg-13-5333-2016-supplement.

Acknowledgements. We thank the captain, crew and shipboard party of the PHOXY cruise aboard R/V *Pelagia* to the Black Sea in June 2013 and G. J. Reichart. We also thank NIOZ Marine Research Facilities for their support and K. Bakker and S. Ossebaar for their contribution to the porewater analysis. D. van de Meent, T. Claessen, T. Zalm, A. van Dijk, E. Dekker and G. Megens are acknowledged for technical and analytical assistance in Utrecht and M. Hagens for her support with the modeling. We further thank C. van der Veen for the methane isotope analysis. This research was funded by ERC Starting Grant 278364, NWO Open Competition Grant 822.01013 and NWO-Vici Grant 865.13.005 (to Caroline P. Slomp). In addition, Peter Kraal would like to acknowledge NWO Veni grant 863.14.014. This work was carried out under the program of the Netherlands Earth System Science Centre (NESSC), financially supported by the Ministry of Education, Culture and Science (OCW). Orit Sivan, Wei-Li Hong and an anonymous reviewer are gratefully acknowledged for their insightful comments and suggestions that improved the quality of the manuscript.

Edited by: T. Treude
Reviewed by: O. Sivan, W.-L. Hong, and one anonymous referee

References

Achtnich, C., Bak, F., and Conrad, R.: Competition for electron donors among nitrate reducers, ferric iron reducers, sulfate reducers, and methanogens in anoxic paddy soil, Biol. Fertil. Soils, 19, 65–72, doi:10.1007/BF00336349, 1995.

Alperin, M. J., Reeburgh, W. S., and Whiticar, M. J.: Carbon and hydrogen isotope fractionation resulting from anaerobic methane oxidation, Global Biogeochem. Cy., 2, 279–288, doi:10.1029/GB002i003p00279, 1988.

Amos, R. T., Bekins, B. A., Cozzarelli, I. M., Voytek, M. A., Kirshtein, J. D., Jones, E. J. P., and Blowes, D. W.: Evidence for iron-mediated anaerobic methane oxidation in a crude oil-contaminated aquifer, Geobiology, 10, 506–517, doi:10.1111/j.1472-4669.2012.00341.x, 2012.

Arthur, M. A. and Dean, W. E.: Organic-matter production and evolution of anoxia in the Holocene Black Sea, Paleoceanography, 13, 395–411, doi:10.1029/98PA01161, 1998.

Beal, E. J., House, C. H., and Orphan, V. J.: Manganese- and iron-dependent marine methane oxidation, Science, 325, 184–187, doi:10.1126/science.1169984, 2009.

Berg, P., Rysgaard, S., and Thamdrup, B.: Dynamic modeling of early diagenesis and nutrient cycling. A case study in an Arctic marine sediment, Am. J. Sci., 303, 905–955, doi:10.2475/ajs.303.10.905, 2003.

Berner, R. A.: Iron sulfides in Pleistocene deep Black Sea sediments and their paleo-oceanographic significance, in: The Black Sea – Geology, Chemistry and Biology, edited by: Degens, E. T. and Ross, D. A., 524–531, Plenum Press, 1974.

Berner, R. A.: Early Diagenesis: A Theoretical Approach, Princeton University Press, 1980.

Bodegom, P. M., Scholten, J. C. M., and Stams, A. J. M.: Direct inhibition of methanogenesis by ferric iron, FEMS Microbiol. Ecol., 49, 261–268, doi:10.1016/j.femsec.2004.03.017, 2004.

Bond, D. R. and Lovley, D. R.: Reduction of Fe(III) oxide by methanogens in the presence and absence of extracellular quinones, Environ. Microbiol., 4, 115–124, doi:10.1046/j.1462-2920.2002.00279.x, 2002.

Boudreau, B. P.: The diffusive tortuosity of fine-grained unlithified sediments, Geochim. Cosmochim. Ac., 60, 3139–3142, doi:10.1016/0016-7037(96)00158-5, 1996.

Boudreau, B. P.: Diagenetic models and their implementation. Modelling transport and reactions in aquatic sediments, Springer, 1997.

Brass, M. and Röckmann, T.: Continuous-flow isotope ratio mass spectrometry method for carbon and hydrogen isotope measurements on atmospheric methane, Atmos. Meas. Tech., 3, 1707–1721, doi:10.5194/amt-3-1707-2010, 2010.

Burns, S. J.: Early diagenesis in Amazon fan sediments, in: Proceeding of the Ocean Drilling Program, Scientific Results, edited by: Flood, R. D., Piper, D. J. W., Klaus, A., and Peterson, L. C., 155, 497–504, 1997.

Burton, E. D., Sullivan, L. A., Bush, R. T., Johnston, S. G., and Keene, A. F.: A simple and inexpensive chromium-reducible sulfur method for acid-sulfate soils, Appl. Geochem., 23, 2759–2766, doi:10.1016/j.apgeochem.2008.07.007, 2008.

Capet, A., Beckers, J.-M., and Grégoire, M.: Drivers, mechanisms and long-term variability of seasonal hypoxia on the Black Sea northwestern shelf – is there any recovery after eutrophication?, Biogeosciences, 10, 3943–3962, doi:10.5194/bg-10-3943-2013, 2013.

Chanton, J., Chaser, L., Glasser, P., and Siegel, D.: Carbon and hydrogen isotopic effects in microbial methane from terrestrial environments, in Stable isotopes and biosphere-atmosphere interactions, edited by: Flanagan, L., Elsevier-Academic Press, Amsterdam, 85–105, 2005.

Claff, S. R., Sullivan, L. A., Burton, E. D., and Bush, R. T.: A sequential extraction procedure for acid sul-

fate soils: Partitioning of iron, Geoderma, 155, 224–230, doi:10.1016/j.geoderma.2009.12.002, 2010.

Crowe, S. A., Katsev, S., Leslie, K., Sturm, A., Magen, C., Nomosatryo, S., Pack, M. A., Kessler, J. D., Reeburgh, W. S., Roberts, J. A., González, L., Douglas Haffner, G., Mucci, A., Sundby, B., and Fowle, D. A.: The methane cycle in ferruginous Lake Matano, Geobiology, 9, 61–78, doi:10.1111/j.1472-4669.2010.00257.x, 2011.

Cruz Viggi, C., Rossetti, S., Fazi, S., Paiano, P., Majone, M., and Aulenta, F.: Magnetite particles triggering a faster and more robust syntrophic pathway of methanogenic propionate degradation, Environ. Sci. Technol., 48, 7536–7543, doi:10.1021/es5016789, 2014.

Degens, E. T. and Ross, D. A.: The Black Sea – geology, chemistry, and biology: American Association of Petroleum Geologists Memoir 20, 1974.

Dijkstra, N., Kraal, P., Kuypers, M. M. M., Schnetger, B., and Slomp, C. P.: Are iron-phosphate minerals a sink for phosphorus in anoxic Black Sea sediments?, PLoS One, 9, e101139, doi:10.1371/journal.pone.0101139, 2014.

Eckert, S., Brumsack, H.-J., Severmann, S., Schnetger, B., März, C., and Frollje, H.: Establishment of euxinic conditions in the Holocene Black Sea, Geology, 41, 431–434, 2013.

Egger, M., Jilbert, T., Behrends, T., Rivard, C., and Slomp, C. P.: Vivianite is a major sink for phosphorus in methanogenic coastal surface sediments, Geochim. Cosmochim. Ac., 169, 217–235, doi:10.1016/j.gca.2015.09.012, 2015a.

Egger, M., Rasigraf, O., Sapart, C. J., Jilbert, T., Jetten, M. S. M., Röckmann, T., van der Veen, C., Bândă, N., Kartal, B., Ettwig, K. F., and Slomp, C. P.: Iron-mediated anaerobic oxidation of methane in brackish coastal sediments, Environ. Sci. Technol., 49, 277–283, doi:10.1021/es503663z, 2015b.

Ettwig, K. F., Butler, M. K., Le Paslier, D., Pelletier, E., Mangenot, S., Kuypers, M. M. M., Schreiber, F., Dutilh, B. E., Zedelius, J., de Beer, D., Gloerich, J., Wessels, H. J. C. T., van Alen, T., Luesken, F., Wu, M. L., van de Pas-Schoonen, K. T., Op den Camp, H. J. M., Janssen-Megens, E. M., Francoijs, K.-J., Stunnenberg, H., Weissenbach, J., Jetten, M. S. M., and Strous, M.: Nitrite-driven anaerobic methane oxidation by oxygenic bacteria, Nature, 464, 543–548, doi:10.1038/nature08883, 2010.

Filippelli, G. M.: Controls on phosphorus concentration and accumulation in oceanic sediments, Mar. Geol., 139, 231–240, 1997.

Froelich, P. N., Klinkhammer, G. P., Bender, M. L., Luedtke, N. A., Heath, G. R., Cullen, D., Dauphin, P., Hammond, D., Hartman, B., and Maynard, V.: Early oxidation of organic matter in pelagic sediments of the eastern equatorial Atlantic: suboxic diagenesis, Geochim. Cosmochim. Ac., 43, 1075–1090, doi:10.1016/0016-7037(79)90095-4, 1979.

Grasshoff, K.: A simultaneous multiple channel system for nutrient analysis in seawater with analog and digital data record, Contrib. 2338, Woods Hole, 1969.

Henkel, S., Mogollón, J. M., Nöthen, K., Franke, C., Bogus, K., Robin, E., Bahr, A., Blumenberg, M., Pape, T., Seifert, R., März, C., de Lange, G. J., and Kasten, S.: Diagenetic barium cycling in Black Sea sediments – A case study for anoxic marine environments, Geochim. Cosmochim. Ac., 88, 88–105, doi:10.1016/j.gca.2012.04.021, 2012.

Hindmarsh, A. C.: ODEPACK, a systematized collection of ODE solvers, in: IMACS Transactions on Scientific Computation, Vol. 1, edited by: Stepleman R. S., and others, North-Holland, Amsterdam, 55–64, 1983.

Holler, T., Wegener, G., Knittel, K., Boetius, A., Brunner, B., Kuypers, M. M. M., and Widdel, F.: Substantial (13) C/(12) C and D/H fractionation during anaerobic oxidation of methane by marine consortia enriched in vitro, Environ. Microbiol. Rep., 1, 370–376, doi:10.1111/j.1758-2229.2009.00074.x, 2009.

Holler, T., Wegener, G., Niemann, H., Ferdelman, T. G., Boetius, A., Kristiansen, T. Z., Molina, H., Pandey, A., Werner, J. K., Juluri, K. R., Xu, Y., Glenn, D., Parang, K., and Snyder, S. H.: Carbon and sulfur back flux during anaerobic microbial oxidation of methane and coupled sulfate reduction, P. Natl. Acad. Sci. USA, 109, 21170–21170, doi:10.1073/pnas.1218683109, 2012.

Holmkvist, L., Ferdelman, T. G., and Jørgensen, B. B.: A cryptic sulfur cycle driven by iron in the methane zone of marine sediment (Aarhus Bay, Denmark), Geochim. Cosmochim. Ac., 75, 3581–3599, doi:10.1016/j.gca.2011.03.033, 2011a.

Holmkvist, L., Kamyshny, A., Vogt, C., Vamvakopoulos, K., Ferdelman, T. G., and Jørgensen, B. B.: Sulfate reduction below the sulfate–methane transition in Black Sea sediments, Deep-Sea Res. Pt. I , 58, 493–504, doi:10.1016/j.dsr.2011.02.009, 2011b.

Holmkvist, L., Kamyshny, A., Brüchert, V., Ferdelman, T. G., and Jørgensen, B. B.: Sulfidization of lacustrine glacial clay upon Holocene marine transgression (Arkona Basin, Baltic Sea), Geochim. Cosmochim. Ac., 142, 75–94, doi:10.1016/j.gca.2014.07.030, 2014.

Hsu, T.-W., Jiang, W.-T., and Wang, Y.: Authigenesis of vivianite as influenced by methane-induced sulfidization in cold-seep sediments off southwestern Taiwan, J. Asian Earth Sci., 89, 88–97, doi:10.1016/j.jseaes.2014.03.027, 2014.

Ingall, E. D., Bustin, R. M., and Van Cappellen, P.: Influence of water column anoxia on the burial and preservation of carbon and phosphorus in marine shales, Geochim. Cosmochim. Ac., 57, 303–316, 1993.

Jilbert, T. and Slomp, C. P.: Iron and manganese shuttles control the formation of authigenic phosphorus minerals in the euxinic basins of the Baltic Sea, Geochim. Cosmochim. Ac., 107, 155–169, doi:10.1016/j.gca.2013.01.005, 2013.

Jørgensen, B. B.: A comparison of methods for the quantification of bacterial sulfate reduction in coastal marine sediments, II. Calculations from mathematical models, Geomicrobiol. J., 1, 29–51, doi:10.1080/01490457809377721, 1978.

Jørgensen, B. B., Weber, A., and Zopfi, J.: Sulfate reduction and anaerobic methane oxidation in Black Sea sediments, Deep-Sea Res. Pt. I , 48, 2097–2120, doi:10.1016/S0967-0637(01)00007-3, 2001.

Jørgensen, B. B., Böttcher, M. E., Lüschen, H., Neretin, L. N., and Volkov, I. I.: Anaerobic methane oxidation and a deep H2S sink generate isotopically heavy sulfides in Black Sea sediments, Geochim. Cosmochim. Ac., 68, 2095–2118, doi:10.1016/j.gca.2003.07.017, 2004.

Kato, S., Hashimoto, K., and Watanabe, K.: Methanogenesis facilitated by electric syntrophy via (semi)conductive iron-oxide minerals, Environ. Microbiol., 14, 1646–1654, doi:10.1111/j.1462-2920.2011.02611.x, 2012.

Kemp, W. M., Testa, J. M., Conley, D. J., Gilbert, D., and Hagy, J. D.: Temporal responses of coastal hypoxia to nutrient loading and physical controls, Biogeosciences, 6, 2985–3008, doi:10.5194/bg-6-2985-2009, 2009.

Knab, N. J., Cragg, B. A., Hornibrook, E. R. C., Holmkvist, L., Pancost, R. D., Borowski, C., Parkes, R. J., and Jørgensen, B. B.: Regulation of anaerobic methane oxidation in sediments of the Black Sea, Biogeosciences, 6, 1505–1518, doi:10.5194/bg-6-1505-2009, 2009.

Knittel, K. and Boetius, A.: Anaerobic oxidation of methane: progress with an unknown process, Annu. Rev. Microbiol., 63, 311–334, doi:10.1146/annurev.micro.61.080706.093130, 2009.

Kraal, P. and Slomp, C. P.: Rapid and extensive alteration of phosphorus speciation during oxic storage of wet sediment samples, PLoS One, 9, e96859, doi:10.1371/journal.pone.0096859, 2014.

Kraal, P., Slomp, C. P., Forster, A., and Kuypers, M. M. M.: Pyrite oxidation during sample storage determines phosphorus fractionation in carbonate-poor anoxic sediments, Geochim. Cosmochim. Ac., 73, 3277–3290, doi:10.1016/j.gca.2009.02.026, 2009.

Leloup, J., Loy, A., Knab, N. J., Borowski, C., Wagner, M., and Jørgensen, B. B.: Diversity and abundance of sulfate-reducing microorganisms in the sulfate and methane zones of a marine sediment, Black Sea, Environ. Microbiol., 9, 131–142, doi:10.1111/j.1462-2920.2006.01122.x, 2007.

Leloup, J., Fossing, H., Kohls, K., Holmkvist, L., Borowski, C., and Jørgensen, B. B.: Sulfate-reducing bacteria in marine sediment (Aarhus Bay, Denmark): abundance and diversity related to geochemical zonation, Environ. Microbiol., 11, 1278–1291, doi:10.1111/j.1462-2920.2008.01855.x, 2009.

Li, H., Chang, J., Liu, P., Fu, L., Ding, D., and Lu, Y.: Direct interspecies electron transfer accelerates syntrophic oxidation of butyrate in paddy soil enrichments, Environ. Microbiol., 17, 1–45, doi:10.1111/1462-2920.12576, 2014.

Liu, D., Wang, H., Dong, H., Qiu, X., Dong, X., and Cravotta, C. A.: Mineral transformations associated with goethite reduction by Methanosarcina barkeri, Chem. Geol., 288, 53–60, doi:10.1016/j.chemgeo.2011.06.013, 2011.

Lovley, D. R.: Dissimilatory Fe(III) and Mn(IV) reduction, Microbiol. Rev., 55, 259–287, 1991.

Lovley, D. R. and Phillips, E. J. P.: Competitive mechanisms for inhibition of sulfate reduction and methane production in the zone of ferric iron reduction in sediments, Appl. Environ. Microbiol., 53, 2636–2641, 1987.

Lovley, D. R., Phillips, E. J. P., and Lonergan, D. J.: Hydrogen and formate oxidation coupled to dissimilatory reduction of iron or manganese by Alteromonas putrefaciens, Appl. Environ. Microbiol., 55, 700–706, 1989.

Martens, C. S., Berner, R. A., and Rosenfeld, J. K.: Interstitial water chemistry of anoxic Long Island Sound sediments, 2. Nutrient regeneration and phosphate removal, Limnol. Oceanogr., 23, 605–617, 1978.

Martens, C. S., Albert, D. B., and Alperin, M. J.: Stable isotope tracing of anaerobic methane oxidation in the gassy sediments of Eckernforde Bay, German Baltic Sea, Am. J. Sci., 299, 589–610, doi:10.2475/ajs.299.7-9.589, 1999.

März, C., Hoffmann, J., Bleil, U., de Lange, G. J., and Kasten, S.: Diagenetic changes of magnetic and geochemical signals by anaerobic methane oxidation in sediments of the Zambezi deep-sea fan (SW Indian Ocean), Mar. Geol., 255, 118–130, doi:10.1016/j.margeo.2008.05.013, 2008.

Meysman, F. J. R., Boudreau, B. P., and Middelburg, J. J.: Modeling reactive transport in sediments subject to bioturbation and compaction, Geochim. Cosmochim. Ac., 69, 3601–3617, doi:10.1016/j.gca.2005.01.004, 2005.

Milucka, J., Ferdelman, T. G., Polerecky, L., Franzke, D., Wegener, G., Schmid, M., Lieberwirth, I., Wagner, M., Widdel, F., and Kuypers, M. M. M.: Zero-valent sulphur is a key intermediate in marine methane oxidation, Nature, 491, 541–546, doi:10.1038/nature11656, 2012.

Mogollón, J. M., Dale, A. W., Jensen, J. B., Schlüter, M., and Regnier, P.: A method for the calculation of anaerobic oxidation of methane rates across regional scales: An example from the Belt Seas and The Sound (North Sea-Baltic Sea transition), Geo-Mar. Lett., 33, 299–310, doi:10.1007/s00367-013-0329-z, 2013.

Moodley, L., Middelburg, J. J., Herman, P. M. J., Soetaert, K., and de Lange, G. J.: Oxygenation and organic-matter preservation in marine sediments: Direct experimental evidence from ancient organic carbon–rich deposits, Geology, 33, 889–892, doi:10.1130/G21731.1, 2005.

Mort, H. P., Slomp, C. P., Gustafsson, B. G., and Andersen, T. J.: Phosphorus recycling and burial in Baltic Sea sediments with contrasting redox conditions, Geochim. Cosmochim. Ac., 74, 1350–1362, doi:10.1016/j.gca.2009.11.016, 2010.

Murphy, J. and Riley, J. P.: A modified single solution method for the determination of phosphate in natural waters, Anal. Chim. Acta, 27, 31–36, doi:10.1016/S0003-2670(00)88444-5, 1962.

Neretin, L. N., Böttcher, M. E., Jørgensen, B. B., Volkov, I. I., Lüschen, H., and Hilgenfeldt, K.: Pyritization processes and greigite formation in the advancing sulfidization front in the Upper Pleistocene sediments of the Black Sea, Geochim. Cosmochim. Ac., 68, 2081–2093, doi:10.1016/S0016-7037(03)00450-2, 2004.

Petzoldt, L. R.: Automatic selection of methods for solving stiff and nonstiff systems of ordinary differential equations, SIAM J. Sci. Stat. Comput., 4, 136–148, doi:10.1137/0904010, 1983.

Poulton, S. and Canfield, D.: Development of a sequential extraction procedure for iron: implications for iron partitioning in continentally derived particulates, Chem. Geol., 214, 209–221, doi:10.1016/j.chemgeo.2004.09.003, 2005.

Qu, D., Ratering, S., and Schnell, S.: Microbial reduction of weakly crystalline iron (III) oxides and suppression of methanogenesis in paddy soil, B. Environ. Contamin. Toxicol., 72, 1172–1181, doi:10.1007/s00128-004-0367-3, 2004.

Raghoebarsing, A. A., Pol, A., van de Pas-Schoonen, K. T., Smolders, A. J. P., Ettwig, K. F., Rijpstra, W. I. C., Schouten, S., Damsté, J. S. S., Op den Camp, H. J. M., Jetten, M. S. M., and Strous, M.: A microbial consortium couples anaerobic methane oxidation to denitrification, Nature, 440, 918–921, doi:10.1038/nature04617, 2006.

Raiswell, R. and Canfield, D. E.: The iron biogeochemical cycle past and present, Geochemical Perspect., 1, 1–220, doi:10.7185/geochempersp.1.1, 2012.

Rayleigh, J. W. S.: Theoretical considerations respecting the separation of gases by diffusion and similar processes, Philos. Mag., 42, 493–499, 1896.

Reeburgh, W.: Oceanic methane biogeochemistry, Am. Chem. Soc., 107, 486–513, doi:10.1021/cr050362v, 2007.

Reed, D. C., Slomp, C. P., and Gustafsson, B. G.: Sedimentary phosphorus dynamics and the evolution of bottom-water hypoxia: A coupled benthic-pelagic model of a coastal system, Lim-

nol. Oceanogr., 56, 1075–1092, doi:10.4319/lo.2011.56.3.1075, 2011a.

Reed, D. C., Slomp, C. P., and de Lange, G. J.: A quantitative reconstruction of organic matter and nutrient diagenesis in Mediterranean Sea sediments over the Holocene, Geochim. Cosmochim. Ac., 75, 5540–5558, doi:10.1016/j.gca.2011.07.002, 2011b.

Regnier, P., Dale, A. W., Arndt, S., LaRowe, D. E., Mogollón, J., and Van Cappellen, P.: Quantitative analysis of anaerobic oxidation of methane (AOM) in marine sediments: A modeling perspective, Earth-Sci. Rev., 106, 105–130, doi:10.1016/j.earscirev.2011.01.002, 2011.

Reiche, M., Torburg, G., and Küsel, K.: Competition of Fe(III) reduction and methanogenesis in an acidic fen, FEMS Microbiol. Ecol., 65, 88–101, doi:10.1111/j.1574-6941.2008.00523.x, 2008.

Rickard, D. and Luther, G. W.: Kinetics of pyrite formation by the H2S oxidation of iron (II) monosulfide in aqueous solutions between 25 and 125° C: The mechanism, Geochim. Cosmochim. Ac., 61, 135–147, doi:10.1016/S0016-7037(96)00322-5, 1997.

Riedinger, N., Formolo, M. J., Lyons, T. W., Henkel, S., Beck, A., and Kasten, S.: An inorganic geochemical argument for coupled anaerobic oxidation of methane and iron reduction in marine sediments, Geobiology, 172–181, doi:10.1111/gbi.12077, 2014.

Rooze, J., Egger, M., Tsandev, I., and Slomp, C. P.: Iron-dependent anaerobic oxidation of methane in coastal surface sediments: potential controls and impact, Limnol. Oceanogr., online first, doi:10.1002/lno.10275, 2016.

Ruttenberg, K. C.: Development of a sequential extraction method for different forms of phosphorus in marine sediments, Limnol. Oceanogr., 37, 1460–1482, 1992.

Ruttenberg, K. C. and Berner, R. A.: Authigenic apatite formation and burial in sediments from non-upwelling, continental margin environments, Geochim. Cosmochim. Ac., 57, 991–1007, doi:10.1016/0016-7037(93)90035-U, 1993.

Sapart, C. J., van der Veen, C., Vigano, I., Brass,, M., van de Wal, R. S. W., Bock, M., Fischer, H., Sowers, T., Buizert, C., Sperlich, P., Blunier, T., Behrens, M., Schmitt, J., Seth, B., and Röckmann, T.: Simultaneous stable isotope analysis of methane and nitrous oxide on ice core samples, Atmos. Meas. Tech., 4, 2607–2618, doi:10.5194/amt-4-2607-2011, 2011.

Scheller, S., Yu, H., Chadwick, G. L., McGlynn, S. E., and Orphan, V. J.: Artificial electron acceptors decouple archaeal methane oxidation from sulfate reduction, Science, 351, 703–707, doi:10.1126/science.aad7154, 2016.

Schulz, H. D., Dahmke, A., Schinzel, U., Wallmann, K., and Zabel, M.: Early diagenetic processes, fluxes, and reaction rates in sediments of the South Atlantic, Geochim. Cosmochim. Ac., 58, 2041–2060, doi:10.1016/0016-7037(94)90284-4, 1994.

Segarra, K. E. A., Comerford, C., Slaughter, J., and Joye, S. B.: Impact of electron acceptor availability on the anaerobic oxidation of methane in coastal freshwater and brackish wetland sediments, Geochim. Cosmochim. Ac., 115, 15–30, doi:10.1016/j.gca.2013.03.029, 2013.

Seifert, R., Nauhaus, K., Blumenberg, M., Krüger, M., and Michaelis, W.: Methane dynamics in a microbial community of the Black Sea traced by stable carbon isotopes in vitro, Org. Geochem., 37, 1411–1419, doi:10.1016/j.orggeochem.2006.03.007, 2006.

Sivan, O., Adler, M., Pearson, A., Gelman, F., Bar-Or, I., John, S. G., and Eckert, W.: Geochemical evidence for iron-mediated anaerobic oxidation of methane, Limnol. Oceanogr., 56, 1536–1544, doi:10.4319/lo.2011.56.4.1536, 2011.

Sivan, O., Antler, G., Turchyn, A. V., Marlow, J. J., and Orphan, V. J.: Iron oxides stimulate sulfate-driven anaerobic methane oxidation in seeps, P. Natl. Acad. Sci. USA, 111, 1–9, doi:10.1073/pnas.1412269111, 2014.

Sivan, O., Shusta, S., and Valentine, D. L.: Methanogens rapidly transition from methane production to iron reduction, Geobiology, 14, 190–203, doi:10.1111/gbi.12172, 2016.

Slomp, C. P., Epping, E. H. G., Helder, W., and Raaphorst, W. Van: A key role for iron-bound phosphorus in authigenic apatite formation in North Atlantic continental platform sediments, J. Mar. Res., 54, 1179–1205, doi:10.1357/0022240963213745, 1996.

Slomp, C. P., Mort, H. P., Jilbert, T., Reed, D. C., Gustafsson, B. G., and Wolthers, M.: Coupled dynamics of iron and phosphorus in sediments of an oligotrophic coastal basin and the impact of anaerobic oxidation of methane, PLoS One, 8, e62386, doi:10.1371/journal.pone.0062386, 2013.

Soetaert, K. and Meysman, F.: Reactive transport in aquatic ecosystems: Rapid model prototyping in the open source software R, Environ. Model. Softw., 32, 49–60, doi:10.1016/j.envsoft.2011.08.011, 2012.

Soetaert, K., Herman, P. M. J., and Middelburg, J. J.: A model of early diagenetic processes from the shelf to abyssal depths, Geochim. Cosmochim. Ac., 60, 1019–1040, doi:10.1016/0016-7037(96)00013-0, 1996.

Soetaert, K., Petzoldt, T., and Meysman, F. J. R.: marelac: Tools for Aquatic Sciences, R Package Version 2.1.3, 2010.

Soulet, G., Delaygue, G., Vallet-Coulomb, C., Böttcher, M. E., Sonzogni, C., Lericolais, G., and Bard, E.: Glacial hydrologic conditions in the Black Sea reconstructed using geochemical pore water profiles, Earth Planet. Sc. Lett., 296, 57–66, doi:10.1016/j.epsl.2010.04.045, 2010.

Soulet, G., Ménot, G., Lericolais, G., and Bard, E.: A revised calendar age for the last reconnection of the Black Sea to the global ocean, Quaternary Sci. Rev., 30, 1019–1026, doi:10.1016/j.quascirev.2011.03.001, 2011.

Stoll, M. H. C., Bakker, K., Nobbe, G. H., and Haese, R. R.: Continous-Flow Analysis of Dissolved Inorganic Carbon Content in Seawater, Anal. Chem., 73, 4111–4116, doi:10.1021/ac010303r, 2001.

Strickland, J. D. and Parsons, T. R.: A Practical Handbook of Seawater Analysis, Bulletin 1, Fisheries Research Board of Canada, Ottawa, Canada, 1972.

Suess, E.: Mineral phases formed in anoxic sediments by microbial decomposition of organic matter, Geochim. Cosmochim. Ac., 43, 339–352, doi:10.1016/0016-7037(79)90199-6, 1979.

Thamdrup, B., Roselló-Mora, R., and Amann, R.: Microbial manganese and sulfate reduction in Black Sea shelf sediments, Appl. Environ. Microbiol., 66, 2288–2297, doi:10.1128/AEM.66.7.2888-2897.2000, 2000.

Treude, T., Krause, S., Maltby, J., Dale, A. W., Coffin, R., and Hamdan, L. J.: Sulfate reduction and methane oxidation activity below the sulfate-methane transition zone in Alaskan Beaufort Sea continental margin sediments: Implications for deep sulfur cycling, Geochim. Cosmochim. Ac., 144, 217–237, doi:10.1016/j.gca.2014.08.018, 2014.

Van Santvoort, P. J. M., De Lange, G. J., Thomson, J., Colley, S., Meysman, F. J. R., and Slomp, C. P.: Oxidation and origin of organic matter in surficial Eastern Mediterranean hemipelagic sediments, Aquat. Geochem., 8, 153–175, doi:10.1023/A:1024271706896, 2002.

Vargas, M., Kashefi, K., Blunt-Harris, E. L., and Lovley, D. R.: Microbial evidence for Fe(III) reduction on early Earth, Nature, 395, 65–67, doi:10.1038/25720, 1998.

Wang, Y. and Van Cappellen, P.: A multicomponent reactive transport model of early diagenesis?: Application to redox cycling in coastal marine sediments, Geochim. Cosmochim. Ac., 60, 2993–3014, doi:10.1016/0016-7037(96)00140-8, 1996.

Wankel, S. D., Adams, M. M., Johnston, D. T., Hansel, C. M., Joye, S. B., and Girguis, P. R.: Anaerobic methane oxidation in metalliferous hydrothermal sediments: influence on carbon flux and decoupling from sulfate reduction, Environ. Microbiol., 14, 2726–2740, doi:10.1111/j.1462-2920.2012.02825.x, 2012.

Whiticar, M. J.: Carbon and hydrogen isotope systematics of bacterial formation and oxidation of methane, Chem. Geol., 161, 291–314, doi:10.1016/S0009-2541(99)00092-3, 1999.

Yoshinaga, M. Y., Holler, T., Goldhammer, T., Wegener, G., Pohlman, J. W., Brunner, B., Kuypers, M. M. M., Hinrichs, K., and Elvert, M.: Carbon isotope equilibration during sulphate-limited anaerobic oxidation of methane, Nat. Geosci., 7, 190–194, doi:10.1038/NGEO2069, 2014.

Zhou, S., Xu, J., Yang, G., and Zhuang, L.: Methanogenesis affected by the co-occurrence of iron(III) oxides and humic substances, FEMS Microbiol. Ecol., 88, 107–120, doi:10.1111/1574-6941.12274, 2014.

Zhuang, L., Xu, J., Tang, J., and Zhou, S.: Effect of ferrihydrite biomineralization on methanogenesis in an anaerobic incubation from paddy soil, J. Geophys. Res.-Biogeo., 120, 876–886, doi:10.1002/2014JG002893, 2015.